

Printing Ferromagnetic Domains in Soft Materials: Mechanism, Modeling, and Applications

by

Yoonho Kim

B.S. Mechanical and Aerospace Engineering
Seoul National University, 2013

Submitted to the Department of Mechanical Engineering
in Partial Fulfillment of the Requirements for the Degree of

Master of Science in Mechanical Engineering

at the

MASSACHUSETTS INSTITUTE OF TECHNOLOGY

June 2018

© 2018 Massachusetts Institute of Technology. All rights reserved.

Signature redacted

Signature of Author.....

.....
Department of Mechanical Engineering
May 23, 2018

Signature redacted

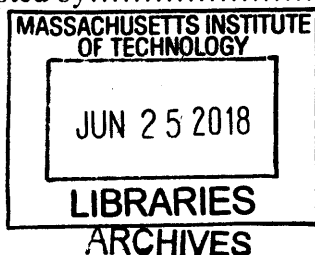
Certified by.....

Xuanhe Zhao
Associate Professor of Mechanical Engineering
Thesis Supervisor

Signature redacted

Accepted by.....

.....
✓ Rohan Abeyaratne
Chairman, Committee on Graduate Students



Printing Ferromagnetic Domains in Soft Materials: Mechanism, Modeling, and Applications

by

Yoonho Kim

Submitted to the Department of Mechanical Engineering
on May 22, 2018 in Partial Fulfillment of the
Requirements for the Degree of Master of Science in
Mechanical Engineering

ABSTRACT

Soft materials capable of transforming between three-dimensional (3D) shapes have applications in areas as diverse as flexible electronics, soft robotics, and biomedicine. This thesis introduces a method of printing ferromagnetic domains in soft materials that yield fast transformation between complex 3D shapes via magnetic actuation. This approach is based on direct ink writing of an elastomer composite containing hard ferromagnetic microparticles. By applying a magnetic field to the dispensing nozzle while printing, we make the particles reoriented along the applied field direction to impart patterned magnetic polarity to printed filaments. This method allows us to design ferromagnetic domains in 3D-printed soft materials encoded with complex programmed shapes. A mathematical model based on a continuum mechanics framework is developed to predict such complex transformation of printed structures under the applied magnetic fields. For this computational model, a constitutive law is developed to describe the behavior of soft materials incorporating hard ferromagnetic microparticles under applied magnetic fields. The capability to quantitatively predict the shape changes enables designing a set of previously inaccessible modes of transformation such as remotely controlled 3D auxetic behaviors in an extremely fast and fully reversible manner via magnetic actuation. The actuation speed and power density of the printed soft materials with programmed ferromagnetic domains are orders of magnitude greater than existing 3D-printed active materials. Diverse functions derived from the fast and complex shape changes such as reconfigurable soft electronics, interaction with quickly moving objects, rolling-based locomotion and delivery of drug pills, and a horizontal leap of a 3D auxetic structure.

Thesis Supervisor: Xuanhe Zhao

Title: Associate Professor of Mechanical Engineering

To my beloved family and dearest Yeong-Eun

ACKNOWLEDGEMENTS

I would not have been able to accomplish all the works presented in this thesis without the help and support of many people. First of all, I thank my advisor, Professor Xuanhe Zhao, for his guidance and support which always encouraged me to pursue creative ideas and broader perspectives while being intellectually engaged during the last one year and a half.

My heartfelt gratitude also goes out to my dear friend, Hyunwoo Yuk. As a senior graduate student in MIT SAMs Lab, he helped me quickly learn many new skills and knowledge required in such multidisciplinary research. Moreover, as a comrade in arms he shared countless exchanges and in-depth discussions not only for research but also on numerous problems and questions we encountered as a graduate student. His commendable enthusiasm for exploring new possibilities through research has been and will become an exemplary model for my professional development.

I also thank Dr. Ruike Zhao, who will start her new journey as a faculty member at Ohio State University, and Professor Shawn A. Chester at New Jersey Institute of Technology for their valuable contributions to the implementation of our finite element model. More specifically, I wish to acknowledge that Ruike spent great efforts on conducting finite element simulations for all demonstrated shape-morphing structures in this thesis.

I thank all my colleagues at MIT SAMs Lab that I had the pleasure of getting to know and having academic discussions. Particular thanks go to Christina Spinelli for her great support and care for all the administrative tasks I encountered while working on my research project.

I thank Dr. David Bono in the Department of Materials Science and Engineering here at MIT for his help in magnetic characterization with the vibrating sample magnetometer. I also wish to thank the Harvard-MIT Division of Health Sciences and Technology for their financial support during the first year of my graduate studies.

Last but not least, I thank my family, friends, and previous teachers for their support and encouragement through the years. I wish to thank my dearest friends Jehyeok and Hyungmook, and my previous academic advisors Prof. Kyujin Cho, Prof. Sung-Hoon Ahn, and Prof. Sun G. Chung at Seoul National University. I especially thank my wonderful girlfriend Yeong-Eun who has been the source of my strength during the challenging period.

TABLE OF CONTENTS

LIST OF FIGURES.....	7
1. INTRODUCTION.....	9
1.1. Shape-programmable Soft Active Materials.....	9
1.2. Magnetically Responsive Soft Materials: Challenges.....	9
1.3. Printing Ferromagnetic Domains in Soft Materials.....	10
1.4. The Scope of the Thesis.....	10
2. PRINTING FERROMAGNETIC DOMAINS IN SOFT MATERIALS.....	11
2.1. Method of Printing Ferromagnetic Domains in Soft Materials.....	11
2.2. Validation of the Printed Ferromagnetic Domains.....	14
2.2.1. Experimental Validation of Magnetization in Printed Samples.....	15
2.2.2. Analytical Interpretation of Magnetization in Printed Samples.....	16
2.3. Design Parameters in the Printing Process.....	18
2.4. Various Designs of Two-dimensional Shape-morphing Structures.....	19
2.5. Support Inks for Printing Three-dimensional Structures.....	22
2.6. Various Designs of Three-dimensional Shape-morphing Structures.....	24
2.7. Materials and Methods.....	27
2.7.1. Ink Compositions and Preparation.....	27
2.7.2. Rheological Characterization.....	28
2.7.3. Magnetic Characterization.....	29
2.7.4. Mechanical Characterization.....	29
3. MODELING OF HARD-MAGNETIC SOFT MATERIALS.....	31
3.1. Introduction.....	31
3.1.1. Magnetoactive Soft Materials.....	31
3.1.2. Soft-magnetic vs Hard-magnetic Materials.....	31
3.1.3. Model-guided Design of Complex Shape-morphing Structures.....	33
3.2. Basic Equations.....	33
3.2.1. Kinematics.....	34
3.2.2. Equilibrium Equations.....	35

3.2.3. Boundary Conditions.....	36
3.3. Constitutive Modeling.....	37
3.3.1. General Form of the Constitutive Relations.....	37
3.3.2. Ideal Hard-magnetic Soft Materials.....	38
3.3.3. Specific Form of the Constitutive Relations.....	41
3.4. Scaling Analysis of Simple Magnetic Actuation.....	43
3.5. Validation of the Computational Model.....	45
3.5.1. Simulation Results vs Analytical Solutions.....	45
3.5.2. Experimental Validation.....	48
4. APPLICATIONS OF PRINTED MAGNETIC SHAPE SHIFTERS.....	50
4.1. Actuation Performance of Printed Shape-shifting Structures.....	50
4.1.1. Energy and Power Densities.....	50
4.1.2. Comparison with Existing 3D-Printed Soft Active Materials.....	51
4.2. Functions and Applications From Programmed Shape Changes.....	53
4.2.1. Reconfigurable Soft Electronics.....	53
4.2.2. Interaction with Fast-moving Objects.....	55
4.2.3. Rolling-based Locomotion and Delivery of Drug Pills.....	55
4.2.4. Horizontal leap of 3D Auxetic Structure.....	58
5. CONCLUSIONS.....	60
6. REFERENCES.....	61

LIST OF FIGURES

Fig. 2.1 Scanning electron microscope images of NdFeB and fume silica particles.....	12
Fig. 2.2 Schematics of the printing process and the material composition.....	12
Fig. 2.3 Rheological properties of composite inks required for printing process.....	13
Fig. 2.4 Micro-computed tomography images of printed fibers.....	13
Fig. 2.5 Demonstration of a single fiber with alternating ferromagnetic domains.....	14
Fig. 2.6 Experimental validation of the magnetization induced during the printing process.....	15
Fig. 2.7 Validation and interpretation of magnetization of printed samples.....	17
Fig. 2.8 Design parameters in the printing process.....	18
Fig. 2.9 Two identical annular rings with different ferromagnetic domains.....	19
Fig. 2.10 Effect of intricate domain patterns on a simple geometry.....	20
Fig. 2.11 Effect of intricate domain patterns on complicated geometries.....	21
Fig. 2.12 Schematic designs and dimensions of 2D planar structures.....	22
Fig. 2.13 Printing of multilayered structures assisted by the use of support inks.....	23
Fig. 2.14 Chemical composition of magnetic and support inks.....	23
Fig. 2.15 Removal of support inks by solvent rinse after curing	24
Fig. 2.16 Multilayered 3D structures with programmed ferromagnetic domains.....	25
Fig. 2.17 Untethered fast-transforming 3D auxetic structure with negative Poisson ratios.....	26
Fig. 2.18 Schematic designs and dimensions of high-aspect-ratio multilayered structures.....	27
Fig. 2.19 Mechanical responses of printed magnetic inks after curing.....	30
Fig. 3.1 Magnetization characteristics of soft-magnetic and hard-magnetic materials.....	32
Fig. 3.2 Model-guided design of printed shape-morphing structures.....	33
Fig. 3.3 Ideal hard-magnetic soft materials characterized by a linear B-H relationship.....	40
Fig. 3.4 A schematic model for scaling analysis of magnetic actuation of a simple beam.....	44
Fig. 3.5 Comparison of the simulations results with analytical solutions.....	48
Fig. 3.6 Experimental validation of finite-element simulations of 2D and 3D structures.....	49
Fig. 4.1 Actuation performance of 3D-printed shape-programmable soft materials.....	52
Fig. 4.2 Exploded and bottom views of the reconfigurable soft electronic device.....	53
Fig. 4.3 Demonstration and mechanism of the reconfigurable soft electronic device.....	54
Fig. 4.4 Demonstration of multiple functions of the printed hexapedal structure.....	56

Fig. 4.5 Demonstration of rolling-based locomotion of the printed hexapedal structure.....	57
Fig. 4.6 Rolling-based delivery of a pharmaceutical dose.....	57
Fig. 4.7 Horizontal leap of a 3D auxetic structure.....	58
Fig. 4.8 Methods of applying magnetic fields to actuate the printed structures.....	59

1. INTRODUCTION

1.1 Shape-programmable Soft Active Materials

Soft materials are in general more favorable to biological systems or human bodies owing to their inherent softness than their rigid counterparts. A class of soft materials that are responsive to external stimuli are called soft active materials. The stimuli to which such materials respond include light, heat, solvent, electric and magnetic fields (1-7). If one can achieve certain desired shapes from such materials, by applying or controlling the external stimuli, those materials are shape-programmable soft active materials. Such soft materials capable of transforming between three-dimensional (3D) shapes in response to external stimuli have attracted great attention due to their emerging applications in areas as diverse as electronic devices (1, 2), soft robotics (3, 4), drug or cell delivery (5, 6), and tissue engineering (7).

1.2 Magnetically Responsive Soft Materials: Challenges

As most biological systems are magnetically transparent, magnetic fields can offer a safe and effective manipulation platform for biomedical applications, which typically require remote actuation in enclosed and confined spaces (8, 9). Another advantage is that magnetic fields and their spatial gradients can be generated independently, which allows decoupling the resulting magnetic torques and forces into two different types of actuation (10). Furthermore, recent progress on spatially selective control of magnetic fields is accelerating the use of magnetic actuation for clinical applications such as targeted drug delivery or adaptive medical implants(10, 11).

Aligned with the advances in magnetic field control, magnetically responsive soft materials have also evolved from embedding discrete magnets (12) or incorporating magnetic particles (13) into soft compounds to generating nonuniform magnetization profiles in polymeric sheets (14, 15). In response to the applied fields, these magnetic soft materials have created multiple modes of locomotion such as crawling, walking, and swimming based on simple bending or undulating deformation under rotating magnetic fields. However, the level of complexity of their shape changes is far lower than is required for many applications, due mainly to the lack of capabilities to create complex 3D structures with soft materials that are encoded with complicated patterns of magnetic domains, which has remained a central challenge in the field.

1.3 Printing Ferromagnetic Domains in Soft Materials

The key concept that passes through the entire thesis is the idea of directly printing magnetic domains in soft materials. Magnetic domains in ferromagnetic materials typically refer to regions in which the magnetization vectors are aligned in the same direction to have overall magnetic polarities in certain directions. Therefore, the concept of printing ferromagnetic domains in soft materials means creating patterns of magnetic polarities in 3D-printed soft materials. This method is based on direct ink writing (16) of an uncured elastomer composite which contains magnetizable microparticles, which, after being magnetized, can be regarded as small permanent magnets. The key idea behind this method is applying a magnetic field on the dispensing nozzle during printing in order to make the magnetized particles reoriented along the applied field direction, which gives rise to patterned magnetic polarity in printed filaments. This new fabrication technique enables designing ferromagnetic domains in 3D-printed soft materials with complex morphologies. After curing, such ferromagnetic soft materials quickly transform into complex 3D shapes upon application of magnetic fields while exhibiting multiple modes of transformation depending on the applied field direction and strength.

1.4 The Scope of the Thesis

This thesis aims to first provide a detailed description of the aforementioned method of printing ferromagnetic domains in soft materials. In Chapter 2, we will identify a few of design parameters which play key roles in the printing process, which are supported by experimental characterizations and analytical interpretations. In the following sections, a variety of examples from one-dimensional to 3D structures which exhibit complex shape changes will be presented with detailed discussions. In Chapter 3, a mathematical model based on a continuum mechanics framework will be developed to quantitatively predict such complex transformations of the printed structures under the applied magnetic fields. In Chapter 4, the actuation performance including the actuation speed and the power density of the printed shape-morphing structures will be evaluated and discussed in comparison with existing 3D-printed active materials based on hydrogels, shape memory polymers, and liquid crystal elastomers.

2. PRINTING FERROMANGETIC DOMAINS IN SOFT MATERIALS

2.1 Method of Printing Ferromagnetic Domains in Soft Materials

The composite ink for 3D printing consists of magnetizable microparticles of neodymium-iron-boron (NdFeB) alloy (Fig. 2.1a) and fumed silica nanoparticles (Fig. 2.1b) embedded in a silicone rubber matrix containing silicone catalyst and crosslinker (Fig. 2.2). The fumed silica within the silicone resin serves as a rheological modifier to induce mechanical properties required for direct ink writing (3, 16) including shear thinning (Fig. 2.3a) and shear yielding (Fig. 2.3b). These properties ensure that the composite ink can be extruded through a micro-nozzle when pressurized and that the deposited inks maintain their shapes even when stacked up to form multiple layers. The composite ink is prepared first by mixing the non-magnetized NdFeB particles and the silica nanoparticles with the uncured elastomer matrix and then magnetized to saturation under an impulse field (~ 2.7 T). The presence of shear yield stress in the composite ink helps prevent the dispersed magnetized particles from agglomerating to form large clusters (Fig. 2.4).

During the printing process, a magnetic field is applied along (or reverse to) the flow direction of the ink via a permanent magnet or an electromagnetic coil placed around the dispensing nozzle (Fig. 2.2). The applied field makes the magnetized NdFeB particles reoriented along the field direction, imparting a permanent magnetic moment to the extruded ink filament. The magnetic polarities of the deposited inks can be tuned either by switching the applied field direction or changing the printing direction. Using this approach, a 3D structure can be encoded with intricate patterns of ferromagnetic domains depending on the magnetic polarities of the filaments that are arranged to construct the 3D structure. To avoid interference in the programmed domains of the printed structure by the applied field at the nozzle, a magnetic shield is used to attenuate the magnetic flux density under the nozzle tip (Fig. 2.2). When the printing process is completed, the printed structure is cured at 120 °C for 1 hr, during which the presence of the shear yield stress in the uncured ink helps the programmed ferromagnetic domains to remain unaffected by thermal randomization of the aligned particles.

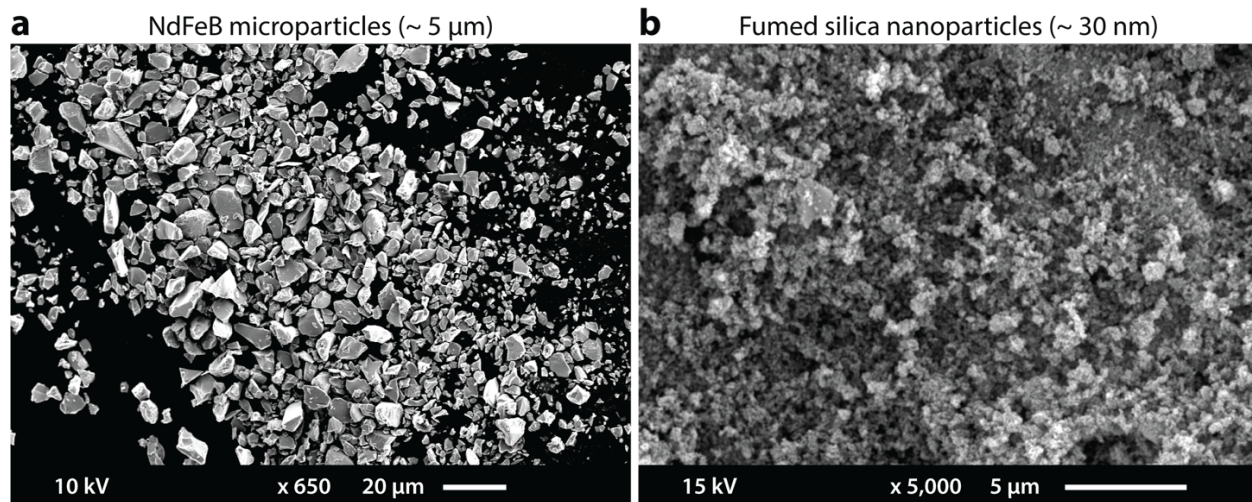


Fig. 2.1 | Scanning electron microscope images of NdFeB and fume silica particles. (a) Magnetizable microparticles of neodymium-iron-boron (NdFeB) alloy in flake-like shapes with an average size of 5 μm and (b) fumed silica nanoparticles with an average size of 30 nm.

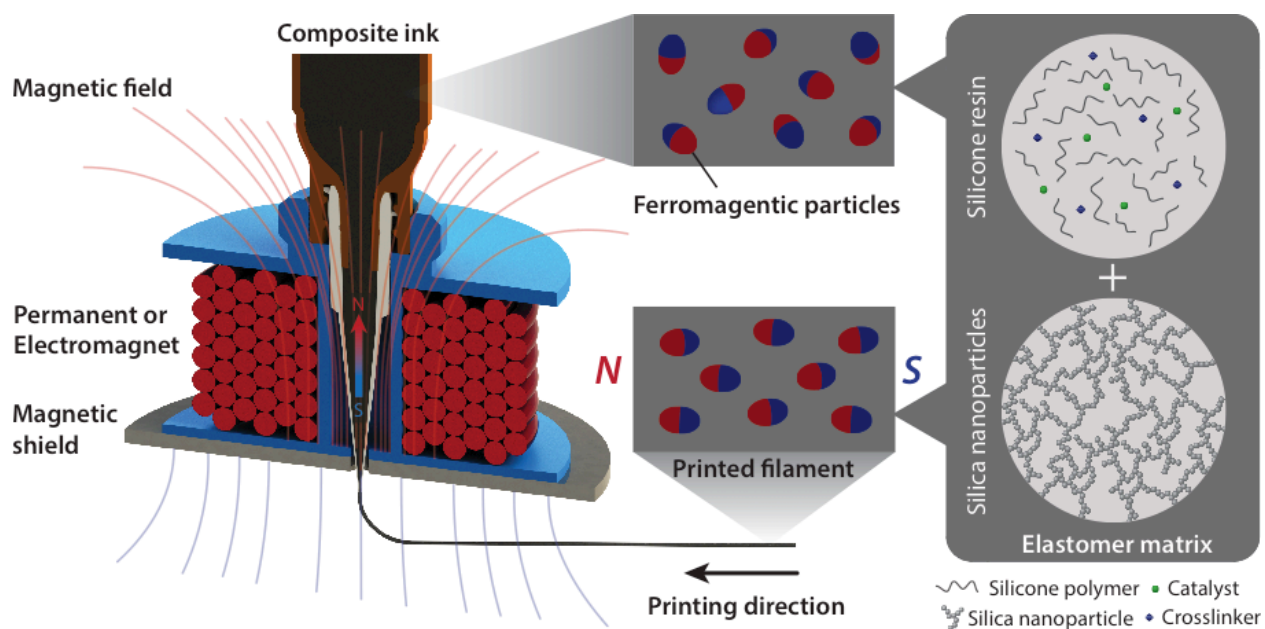


Fig. 2.2 | Schematics of the printing process and the material composition. The magnetized microparticles embedded in the elastomer matrix of the composite ink are reoriented by the applied magnetic field generated by a permanent magnet or an electromagnet placed around the dispensing nozzle.

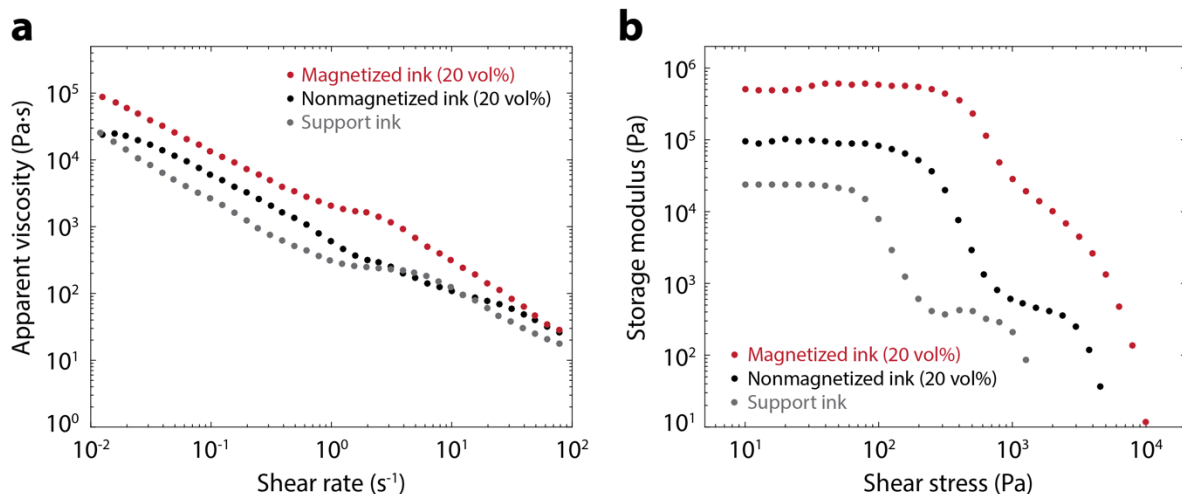


Fig. 2.3 | Rheological properties of composite inks required for printing process. (a) Apparent viscosity as a function of applied shear rate and (b) storage modulus as a function of applied shear stress (b) for 20 vol% magnetized ink (red), 20 vol% nonmagnetized ink (black), and support ink (gray).

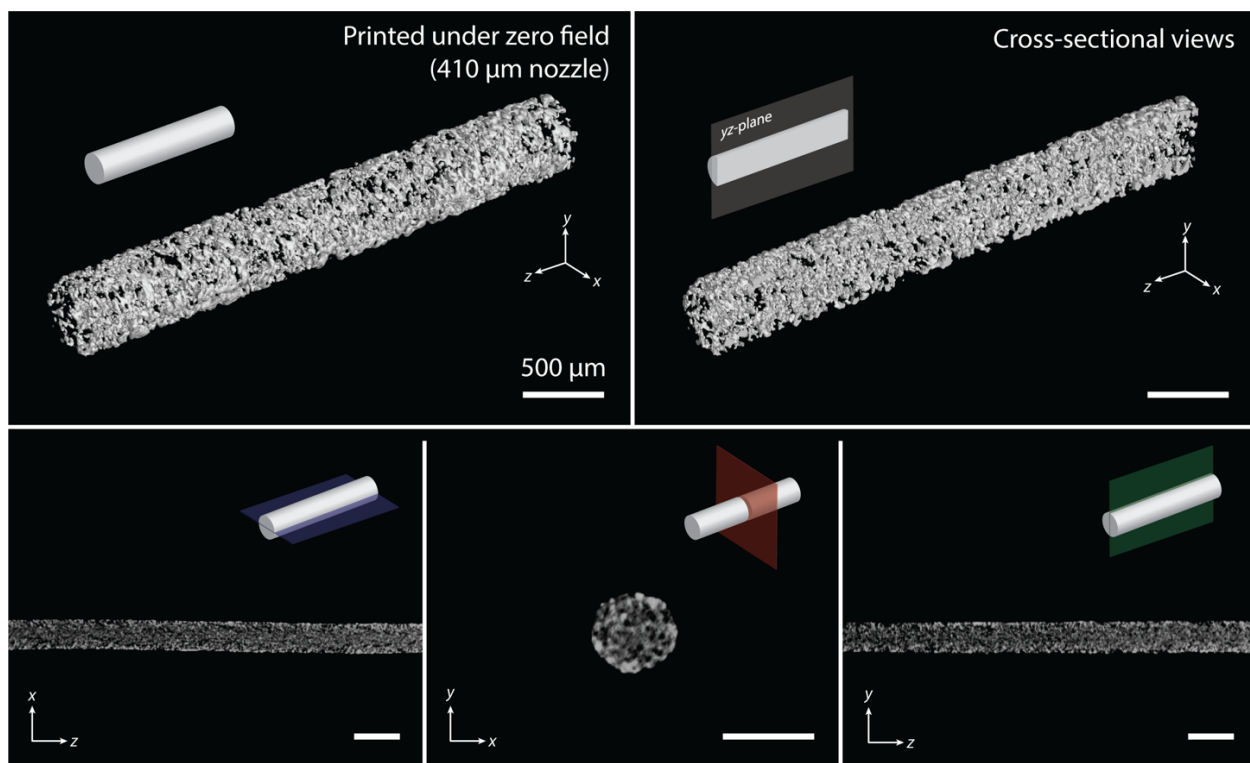


Fig. 2.4 | Micro-computed tomography images of printed fibers. A fiber printed with 410 μm -diameter nozzle in the absence of applied magnetic field. No obvious agglomeration of embedded magnetic microparticles in the printed fibers is observed.

2.2 Validation of Printed Ferromagnetic Domains

As an illustrative example to demonstrate the ability to program ferromagnetic domains, a straight filament is printed with an alternating magnetization pattern as illustrated in Fig. 2.5 by switching the applied field direction during the printing. Upon application of a uniform magnetic field (200 mT), the straight filament transforms into an “m” shape in 0.1 s (Fig. 2.5), due to the torques generated by the particles in printed ferromagnetic domains, and quickly reverts to its original shape upon removal of the applied field in 0.2 s. Such rapid, reversible transformation can be repeated on demand by magnetic actuation. The simulation conducted in the same conditions, including the magnetic and mechanical properties and the applied field as in the experiment, is in good agreement with the experimental results (Fig. 2.5), validating the use of model-based simulation to guide the design of complex shape-morphing structures with programmed ferromagnetic domains. Details about the computational model and the model-based simulation will be discussed in Section 3.

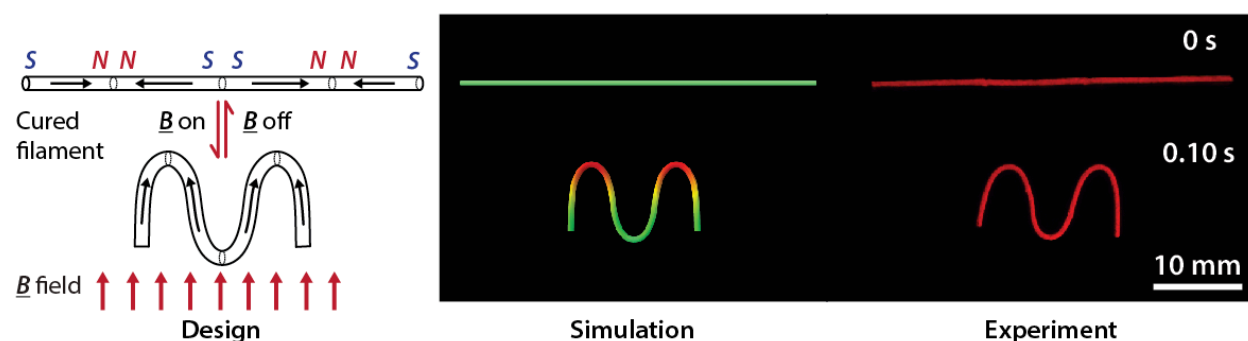


Fig. 2.5 | Demonstration of a single fiber with alternating ferromagnetic domains. The printed fiber is designed to form an ‘m’ shape in 0.1 s under an applied magnetic field of 200 mT. The elastomeric fiber is printed using a nozzle of diameter 840 μm while switching the direction of magnetic fields (50 mT at the nozzle tip) generated by an electromagnetic coil that encompasses the nozzle.

2.2.1 Experimental Validation of Magnetization in Printed Samples

The magnetization of a sample printed with a 410 μm nozzle in the presence of magnetic fields (50 mT) was measured while varying the angular position of the printed fibers with respect to the horizontal direction (Fig. 2.6a). The maximum magnetization value was measured when the printed fibers are aligned with the positive x -direction, in which an external magnetic field is applied by the vibrating sample magnetometer. The measured magnetization value decreased as the angle increased and reached almost zero when the printed fibers were vertically aligned. When the specimen was rotated by 180 degrees, the sign of the measured magnetization was changed, indicating that the specimen's magnetic polarity was reversed, while the magnitude remained almost unchanged (Fig. 2.6b). This data demonstrates that the printed fiber direction can represent the overall magnetization direction (magnetic polarity) of the printed sample.

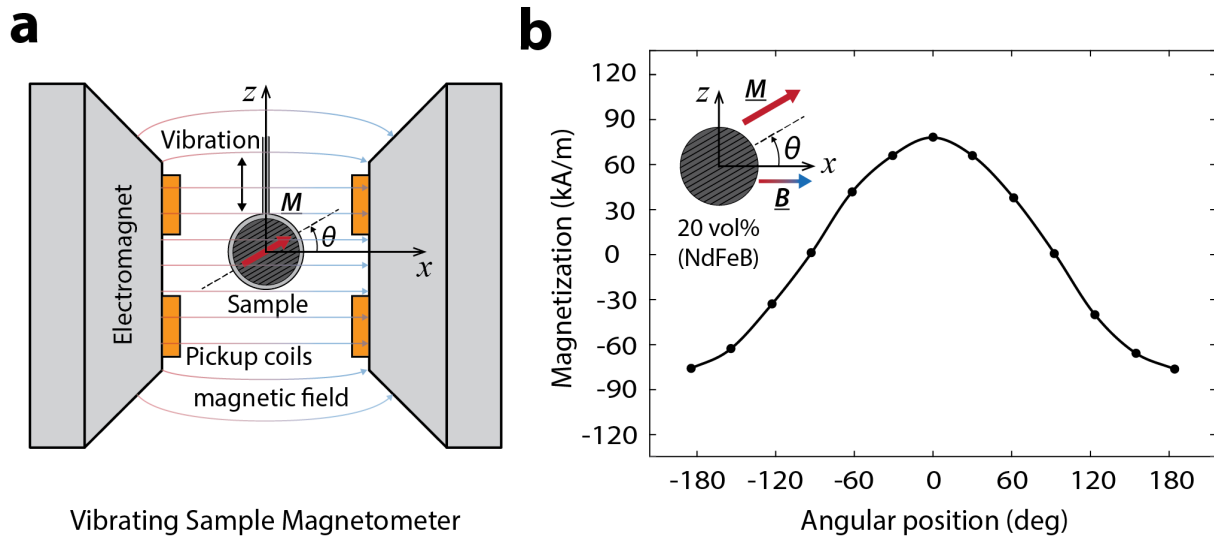


Fig. 2.6 | Experimental validation of the magnetization induced during the printing process.

(a) Experimental setup with a vibrating sample magnetometer for validating the direction of magnetization of a sample printed with a 410 μm nozzle under the presence of magnetic fields (50 mT). (b) Magnetization values measured while varying the angular position of the printed fibers with respect to the external magnetic field applied by the vibrating sample magnetometer.

2.2.2 Analytical Interpretation of Magnetization in Printed Samples

When external fields are applied at the nozzle during the printing process, the ferromagnetic particles embedded in the composite ink are reoriented along the applied field direction, forming angular distributions of magnetic dipole moments, which collectively lead to the overall magnetization of the printed samples. The quality of alignment of the ferromagnetic particles is thus characterized by measuring the magnetic moment density of the printed samples after curing. The measured magnetization value M at certain volume fraction of the NdFeB particles can be interpreted as the summed effect of magnetic moments of the embedded particles per unit volume, whose angular positions relative to the printing direction can be assumed to follow a normal distribution. In other words, the magnetization value can be translated into the standard angular deviation of the magnetic dipole moments \mathbf{m} of particles relative to the direction of overall magnetization \mathbf{M} of the printed samples.

For a printed sample with volume V incorporating N ferromagnetic particles, the magnetization M can be mathematically expressed as

$$M = \frac{1}{V} \int_{-\pi}^{\pi} NP(\theta)M_p\bar{V}_p \cos\theta d\theta, \quad (2.1)$$

where M_p represents the saturation magnetization of NdFeB; \bar{V}_p the mean volume of a single particle; and $P(\theta)$ the probability density function for Gaussian distributions with θ representing the angular deviation of the magnetic dipole moment ($\mathbf{m} = \mathbf{M}_p\bar{V}_p$) of the particle of interest with respect to the printing direction, which corresponds to the direction of overall magnetization \mathbf{M} . Then, for a certain particle volume fraction φ , which corresponds to $\varphi = N\bar{V}_p / V$, the magnitude of the magnetization vector \mathbf{M} , denoted as a scalar quantity M , can be expressed as

$$M = 2\varphi M_p \int_0^{\pi} \frac{1}{\sqrt{2\pi\sigma^2}} e^{-\frac{\theta^2}{2\sigma^2}} \cos\theta d\theta, \quad (2.2)$$

with σ representing the standard deviation of the normal distribution. This equation directly relates the measured magnetization M of the printed samples to the angular distribution of the magnetic dipoles that are aligned by the external field applied during the printing process. As a result, we can draw curves describing the angular distribution of magnetic dipoles in the printed samples ($\varphi = 0.2$) with different magnetization values as shown in Fig. 2.7b.

In a uniformly magnetized sample (Fig. 2.7a), however, which yields the maximum achievable magnetization at the designated volume fraction of NdFeB particles, all magnetic dipole moments (\mathbf{m}) are pointing the same direction as the overall magnetization vector \mathbf{M} . For the calculation of the standard deviation σ that corresponds to the magnetization value M , $M_p = 650$ kA/m is used for the saturation magnetization as the material property of the NdFeB particles used in this study. When the inks are printed in the absence of external field and then magnetized under impulse fields (~ 2.7 T) after curing, maximum magnetization can be achieved at each volume fraction of NdFeB particles. When compared with this method, printing with nozzles of diameter $410\ \mu\text{m}$ under magnetic fields of 50 mT yields magnetization that corresponds to $63\sim 64\%$ of the maximum achievable value at the same concentration of NdFeB particles (Fig. 2.7a). As discussed above, the gap between the attained magnetic moment density and the maximum achievable magnetization can be attributed to the angular deviation of the NdFeB particles within the printed samples relative to the applied field direction under the assumption of Gaussian distributions (Fig. 2.7b).

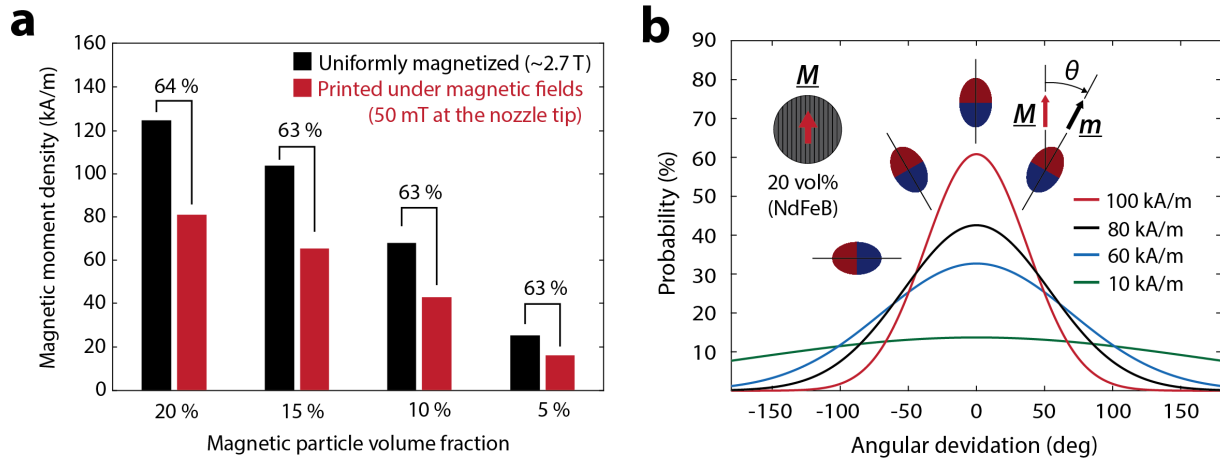


Fig. 2.7 | Validation and interpretation of magnetization of printed samples. (a) Magnetic moment densities of printed samples with different NdFeB particle volume fractions, which correspond to $63\sim 64\%$ of the maximum achievable magnetization at each volume fraction. (b) Analytical interpretation of magnetization values of printed samples as angular distribution of magnetic dipole moments.

2.3 Design Parameters in the Printing Process

To evaluate the efficacy of the proposed method in printing ferromagnetic domains, we measured the magnetic moment density, or magnetization, in samples printed under various conditions such as the magnetic particle content, the applied field strength, and the nozzle diameter. First, samples are printed with magnetic inks containing different volume fractions of NdFeB particles through a nozzle with a diameter of 0.41 mm under magnetic fields of 50 mT at the nozzle tip. The measured magnetic moment density varies almost linearly from 16 to 81 kA/m as the volume fraction of NdFeB particles in the composite ink increases from 5 to 20 % (Fig. 2.8). Next, as the applied field at the nozzle tip increases from 20 to 50 mT, the magnetic moment density of printed samples (with 20 vol% NdFeB particles through nozzles with 0.41-mm diameter) increases from 68 to 81 kA/m (Fig. 2.8). When the nozzle diameter varies from 210 to 1190 μm , the magnetic moment density of printed samples (with 20 vol% NdFeB particles under 50-mT field at the nozzle tip) increases from 70 to 86 kA/m (Fig. 2.8). Printing in the absence of external magnetic fields, however, yields magnetization values below 5 kA/m for all nozzle diameters due to randomly oriented particles.

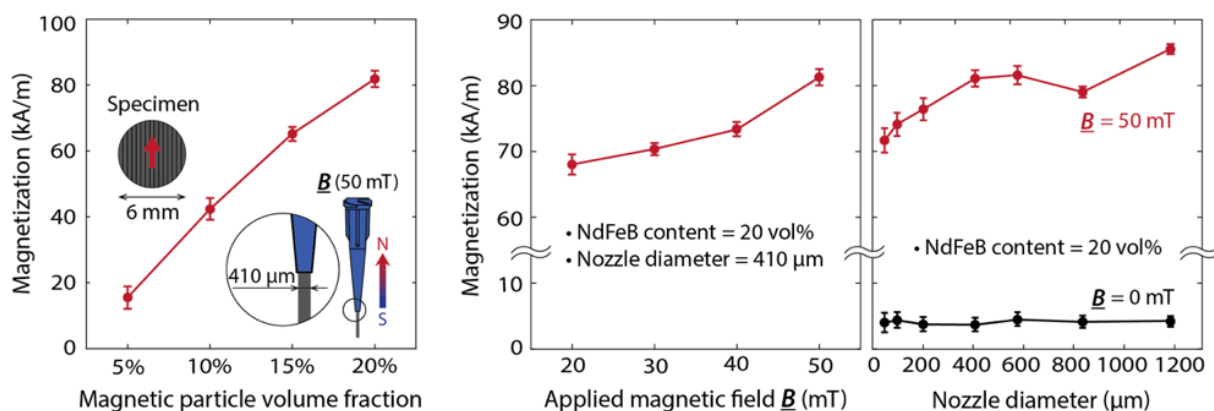


Fig. 2.8 | Design parameters in the printing process. Effects of the volume fraction of magnetized NdFeB particles, the applied field strength, and the nozzle diameter on the magnetization of printed samples. Samples printed in the absence of applied magnetic fields give magnetization values below 5 kA/m. Error bars indicate the standard deviation for $n = 3$ measurements at each data point.

2.4 Various Designs of Two-dimensional Shape-morphing Structures

In this section, we present a set of two-dimensional (2D) planar structures that rapidly transform into complex 3D shapes under the applied magnetic fields (200 mT) due to the programmed ferromagnetic domains. In Fig. 2.9 a and d, we design two annular rings with the same geometry but different patterns of ferromagnetic domains to illustrate the effects of programmed domains on the macroscale response. Our model-based simulation predicts that the two rings yield different 3D morphologies under the same magnetic field applied perpendicularly to their planes. The second annulus encoded with alternating patterns that vary in magnitude gives a more complex undulating shape (Fig. 2.9e) compared to the first annulus (Fig. 2.9b) whose alternating patterns are equidistant. The simulation results are in good agreement with experimental results (Fig. 2.9 c and f), further demonstrating that our model is capable of guiding the design of complex shape-morphing structures based on programming ferromagnetic domains.

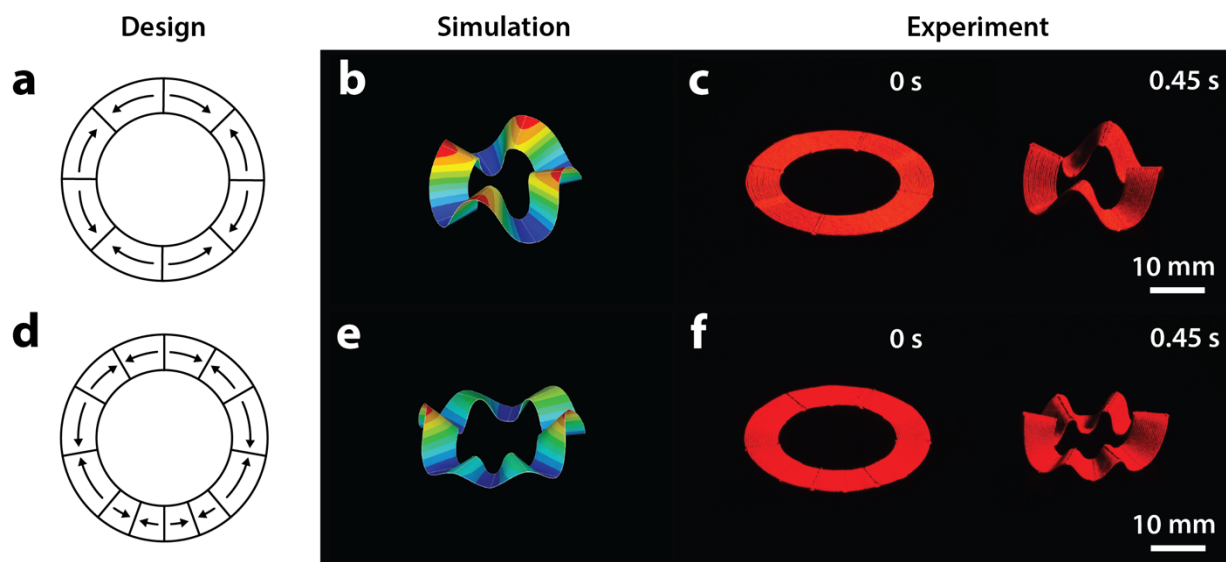


Fig. 2.9 | Two identical annular rings with different ferromagnetic domains. Schematic designs, finite-element simulations, and experimental results of an annulus encoded with alternating domains that are equidistant (a-c) and an annulus encoded with alternating domains that vary in size (d-f).

When programmed with more intricate domain patterns, even a simple geometry can yield a complex 3D shape under an applied magnetic field. As an example, in Fig. 2.10a, we design a simple rectangular structure with alternating oblique patterns of ferromagnetic domains to create a Miura-ori pattern (17). This untethered structure gives fast (in 0.3 s) and fully reversible folding/unfolding under magnetic actuation (Fig. 2.10c), as predicted by our model (Fig. 2.10b). Notably, the response speed of our Miura-ori structure with programmed ferromagnetic domains is much faster than existing ones in the literature based on liquid crystal elastomers (18, 19), shape memory polymers (20, 21), and thermally responsive hydrogels (22).

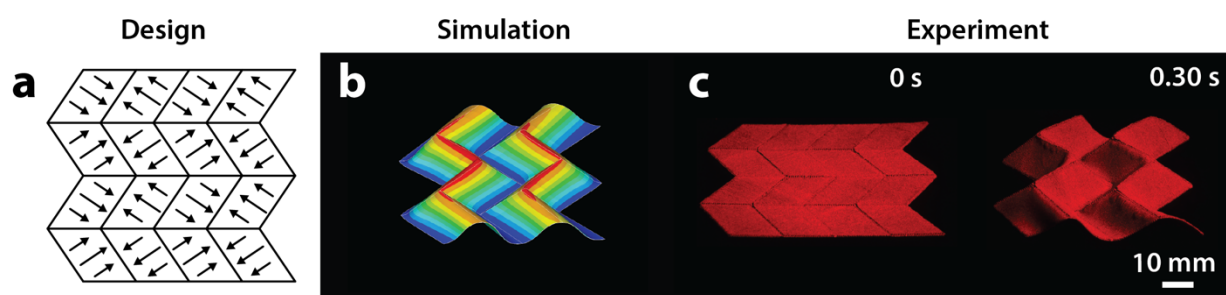


Fig. 2.10 | Effect of intricate domain patterns on a simple geometry. (a) Schematic designs (b), finite-element simulations, and (c) experimental results of a Miura-ori fold encoded with alternating oblique patterns of ferromagnetic domains.

When more intricate designs are programmed with ferromagnetic domains, as illustrated in Fig. 2.11, a, d, and g, the 2D planar structures transform into more complex 3D shapes (Fig. 2.11, c, f, and i) that are no longer straightforward to trace their original shapes without knowing the programmed domains. Design and realization of such complex shape-morphing structures are enabled by the model-based simulations which accurately predict the complex 3D morphologies that are revealed by experiments (Fig. 2.11, b, e, and f). Previously, a transition from 2D planar structures to complex 3D shapes has been achieved by controlled buckling of materials that are selectively attached on biaxially stretched elastomeric substrates (23, 24). When compared with existing techniques, our method based on printing ferromagnetic domains offers additional advantages in 2D to 3D structural transition, including (i) substrate-free, remote actuation, (ii) fast and fully reversible transformation, and (iii) the capability to selectively actuate specific parts of the structure.

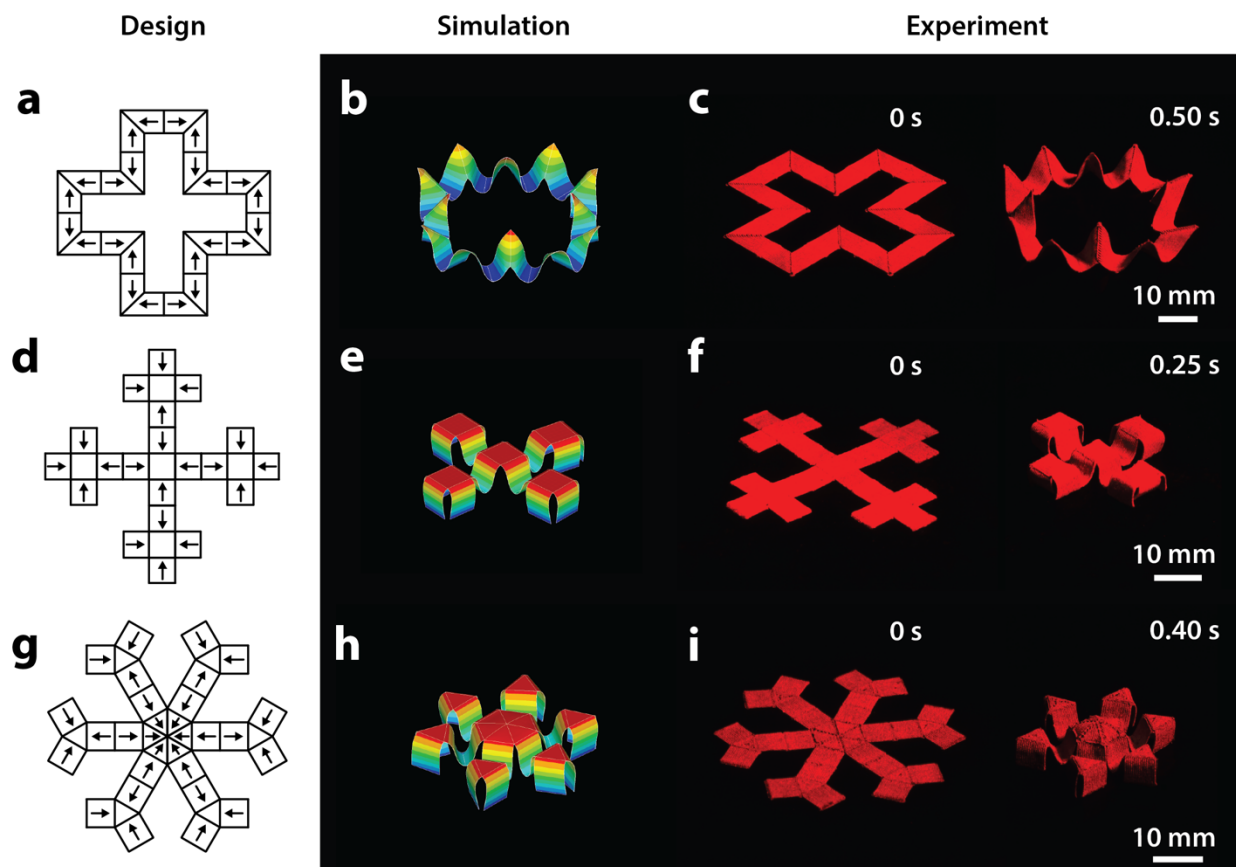


Fig. 2.11 | Effect of intricate domain patterns on complicated geometries. Schematic designs, finite-element simulations, and experimental results of a hollow cross encoded with alternating ferromagnetic domains along the perimeter (a-c); quadrupedal (d-f) and hexapedal (g-i) structures enabled by folding of the magnetically active segments surrounding the magnetically inactive segments (unlabeled areas in the schematic designs).

All demonstrated structures are printed with the elastomeric composite ink containing 20 vol% of magnetized NdFeB particles using a nozzle with 410- μm diameter under the magnetic field of 50 mT at the nozzle tip generated by a permanent magnet. Actuation of the demonstrated structures is performed by applying magnetic fields of 200 mT perpendicular to the planes of the structures. The detailed dimensions of the printed structures are given in Fig. 2.12.

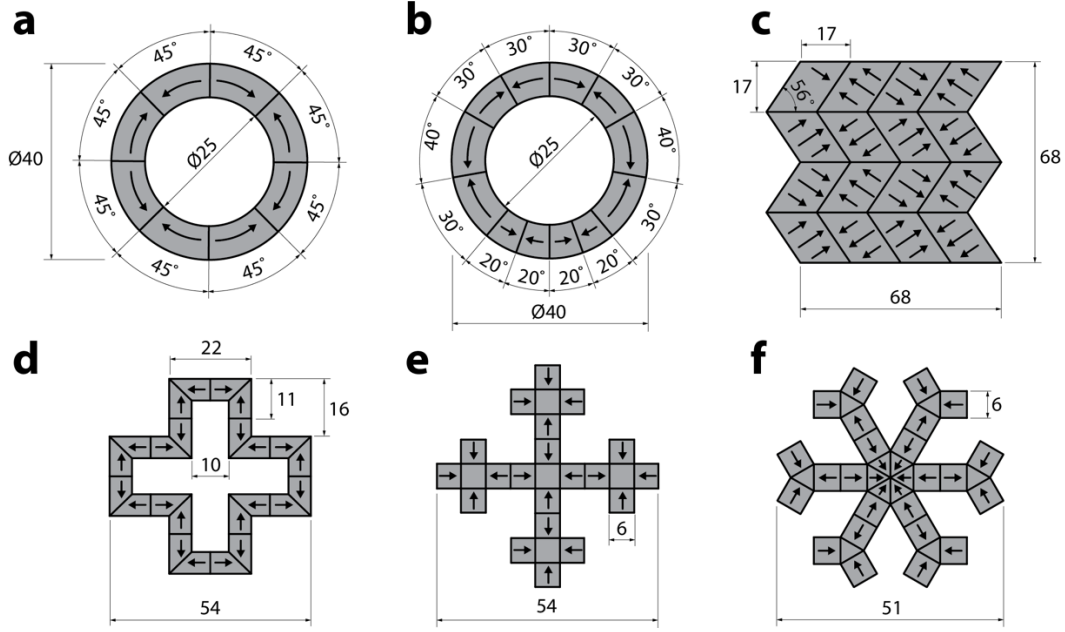


Fig. 2.12 | Schematic designs and dimensions of 2D planar structures. (a) An annulus encoded with alternating domains that are equidistant; (b) an annulus encoded with alternating domains that vary in size; (c) a Miura fold encoded with alternating oblique patterns of ferromagnetic domains; (d) a hollow cross encoded with alternating ferromagnetic domains along the perimeter; and (e) quadrupedal and (f) hexapedal pop-up structures enabled by folding of the magnetically active segments surrounding the magnetically inactive segments.

2.5 Support Inks for Printing Three-dimensional Structures

Our method of printing ferromagnetic domains can be further extended to complex 3D structures. When printing 3D structures with direct ink writing, however, difficulties typically arise due to increasing structural instability as the deposited filaments are stacked up. To ensure a more stable printing process, we introduce support ink composed of a silicone resin containing catalyst and fumed silica nanoparticles (Fig. 2.14; see Fig. 2.3 for rheological properties). When printed, the support ink serves as a fugitive support that buttresses the adjacent magnetic ink (Fig. 2.13). After the magnetic ink is fully cured, the support ink can be removed by solvent rinses (Fig. 2.15). The use of support ink and the consequent ability to print 3D structures with programmed domains allow us to create a set of high-aspect-ratio multilayered structures that exhibit rapid and reversible transformation between complex 3D shapes under magnetic fields, which will be presented in the following section.

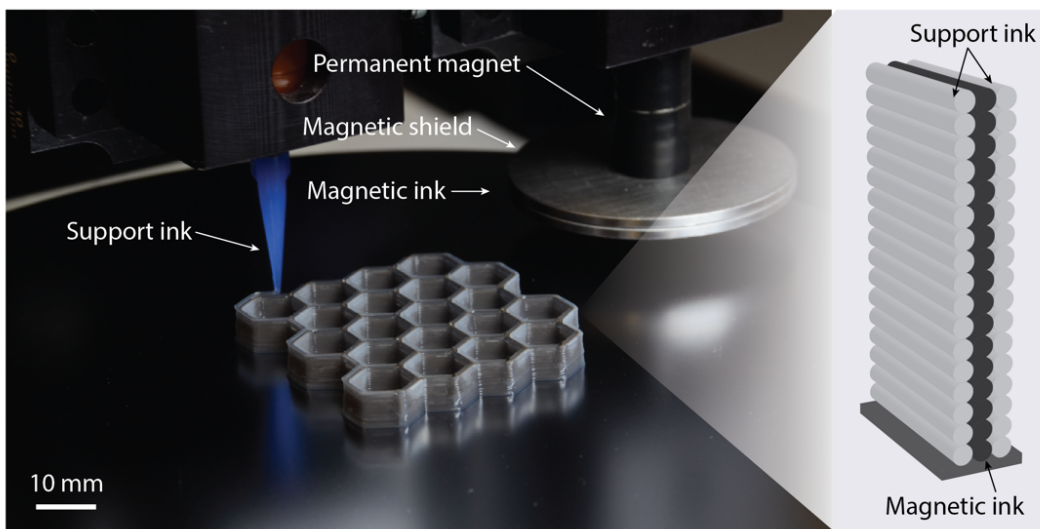


Fig. 2.13 | Printing of multilayered structures assisted by the use of support inks. Printing multilayered hexagonal arrays using magnetic and support inks. The use of support inks as fugitive buttresses enables stacking the deposited magnetic inks stably up to tens or even hundreds of layers.

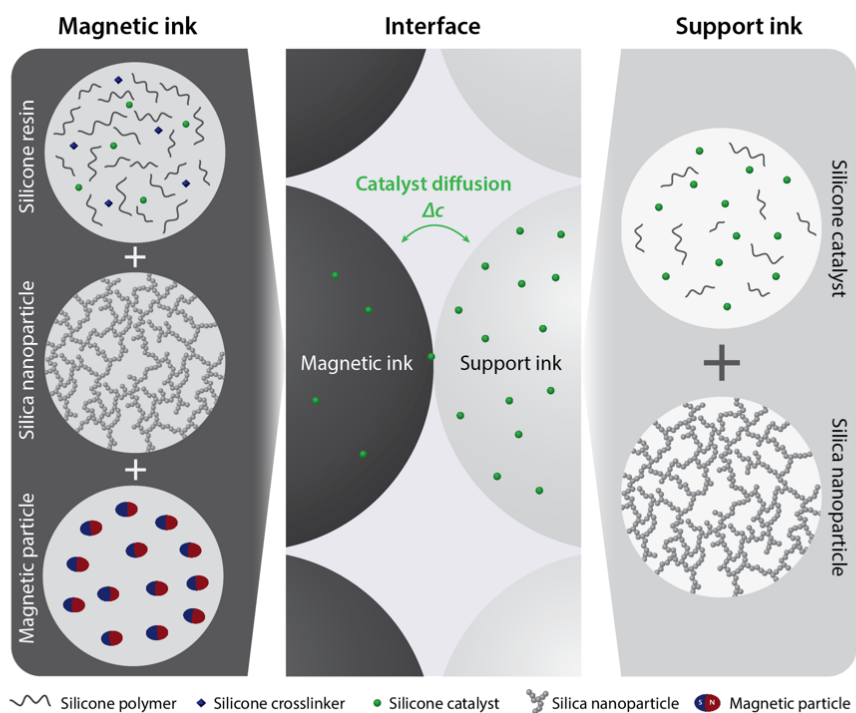


Fig. 2.14 | Chemical composition of magnetic and support inks. The higher concentration of catalyst in the support ink prevents diffusion of catalyst molecules through the interface and thus prevents imperfect curing of the adjacent magnetic inks.

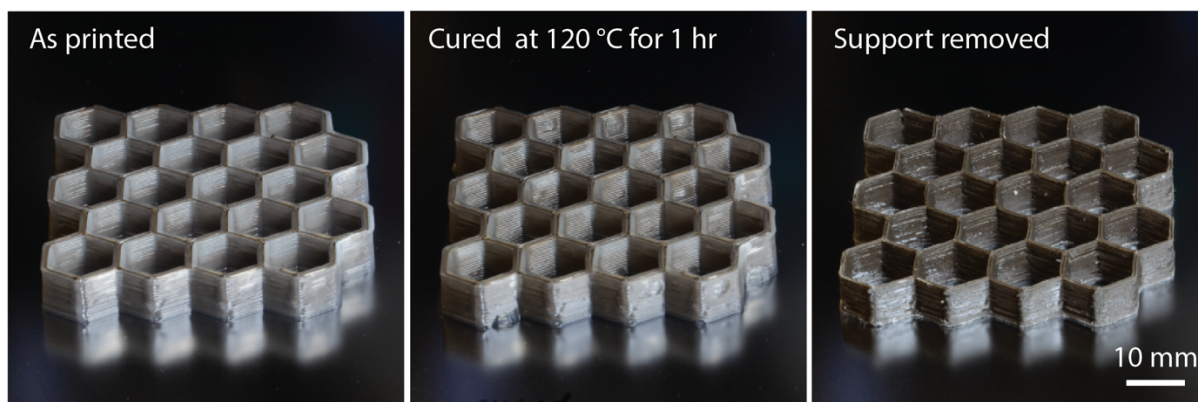


Fig. 2.15 | Removal of support inks by solvent rinse after curing. The printed magnetic inks are cured by heating at 120 °C for 1 hr. The support ink is then removed by solvent rinses.

2.6 Various Designs of Three-dimensional Shape-morphing Structures

In this section, we present a variety of fully 3D structures with programmed ferromagnetic domains, which are enabled by the use of support ink and the consequent ability to stack up the printed magnetic inks up to tens or even hundreds of layers. Fig. 2.16c shows a thin-walled structure consisting of two adjoining hexagonal tubes with high aspect ratios. The ferromagnetic domains are programmed in a way that some parts of the tubes expand while the others collapse, as illustrated in Fig. 2.16a, to create complex undulating surfaces in a continuous 3D structure under the applied magnetic field, as predicted and observed by the simulation and the experiment (Fig. 2.16 b and c), respectively. As another example to demonstrate the versatility of our fabrication method, we create a pyramid-shaped thin-walled structure that elongates along the direction of applied magnetic fields (Fig. 2.16 e and f) due to the programmed magnetic domains (Fig. 2.16d).

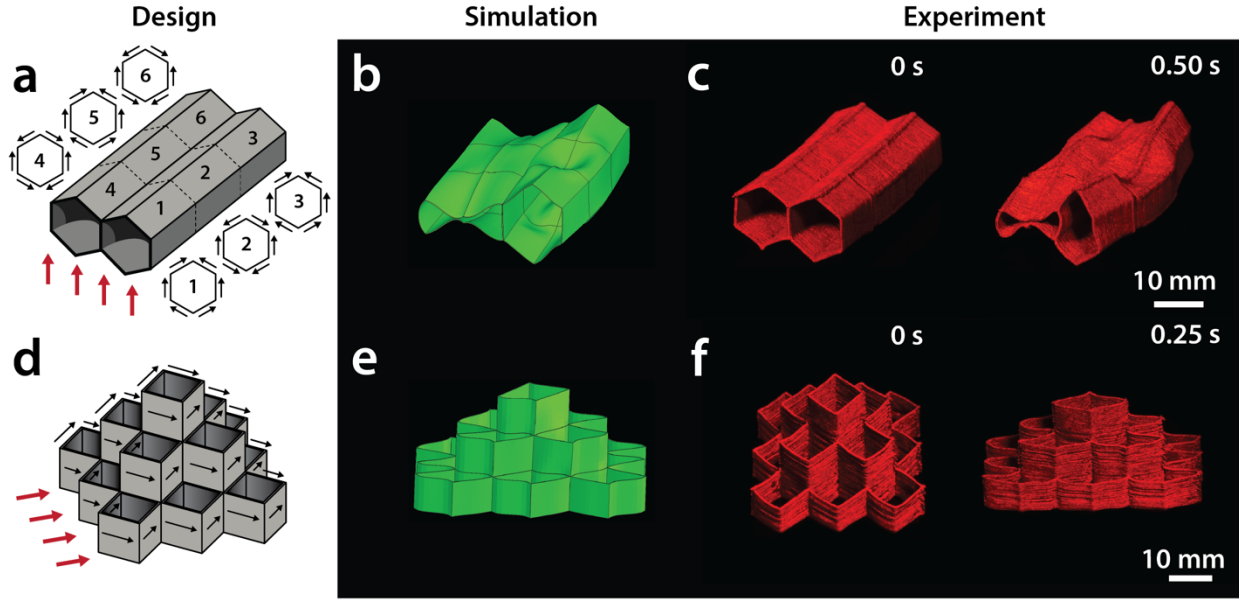


Fig. 2.16 | Multilayered 3D structures with programmed ferromagnetic domains. Schematic designs, finite-element simulations, and experimental results of (a-c) two adjoining hexagonal tubes programmed to form undulating surfaces under external magnetic fields due to the alternating ferromagnetic domains and (d-f) a pyramid-shaped thin-walled structure exhibiting elongation in its diagonal direction along the applied external fields.

The versatility of our model-guided design and fabrication method enables us to create mechanical metamaterials (Fig. 2.17, c, f, and i), so-called auxetic structures characterized by the negative Poisson's ratios, which exhibit shrinkage in both length and width in response to external magnetic fields. Typically, mechanical metamaterials show auxetic behaviors only when uniaxially compressed or stretched and thus require direct mechanical contact (25). In addition, due to the limited fabrication techniques to achieve complex designs, remote actuation of untethered auxetic structures has not been realized by other types of active materials. Guided by our model-based predictions (Fig. 2.17, b, e, and f), we design a set of mechanical metamaterials with programmed ferromagnetic domains (Fig. 2.17, a, d, and g) that quickly shrink under the applied fields within 0.5 s and recover their original shapes upon removal of the applied fields (Fig. 2.17, c, f, and i). The use of magnetic fields as an actuation method obviates the need for direct contact in realizing auxetic behaviors of mechanical metamaterials.

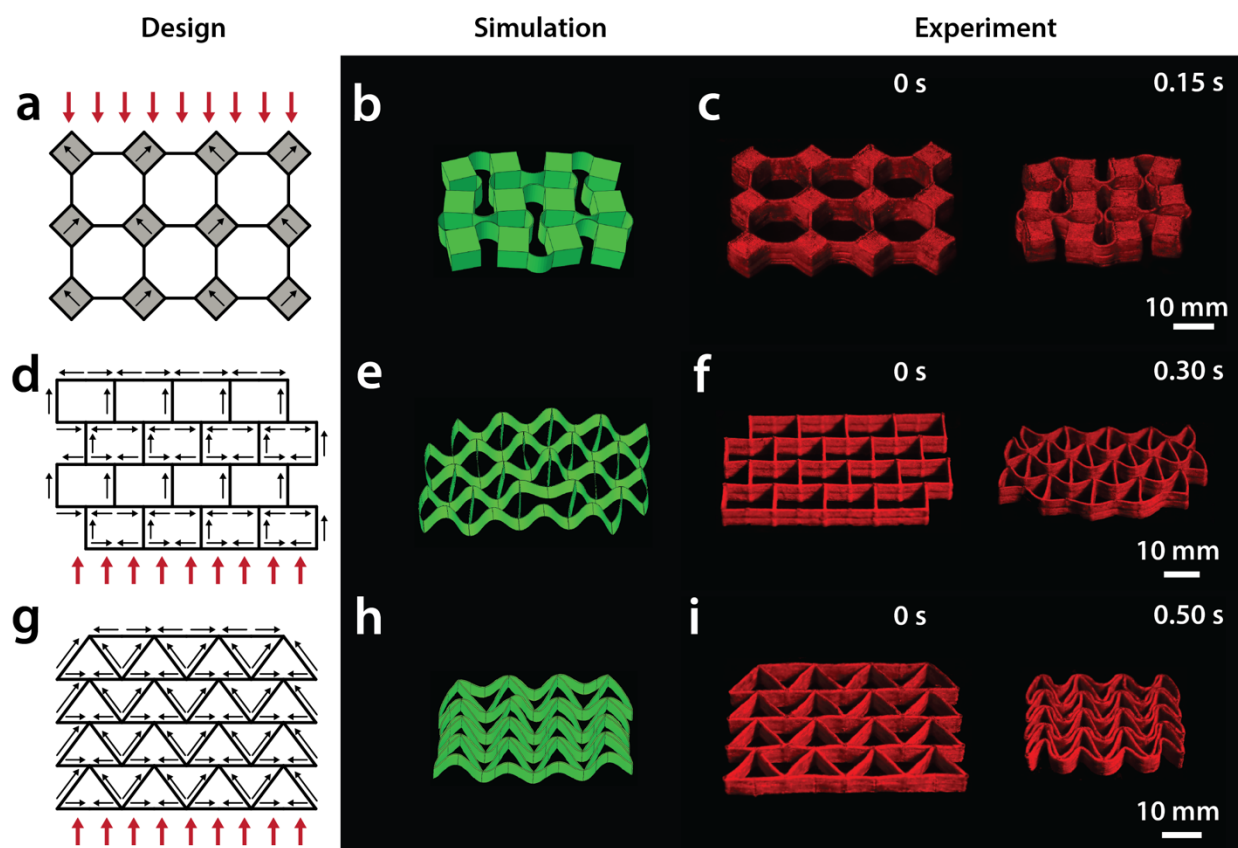


Fig. 2.17 | Untethered fast-transforming 3D auxetic structures with negative Poisson's ratios.

Schematic designs, finite-element analysis predictions, and experimental results of a set of auxetic structures with negative Poisson's ratios exhibiting shrinkage in both length and width under external magnetic fields.

All demonstrated 3D structures are printed with the elastomeric composite ink containing 20 vol% of magnetized NdFeB particles using a nozzle with 410- μm diameter under the magnetic field of 50 mT at the nozzle tip generated by a permanent magnet. Actuation of the demonstrated structures is performed by applying magnetic fields of 200 mT perpendicular to the planes of the structures. The detailed dimensions of the printed structures are given in Fig. 2.18.

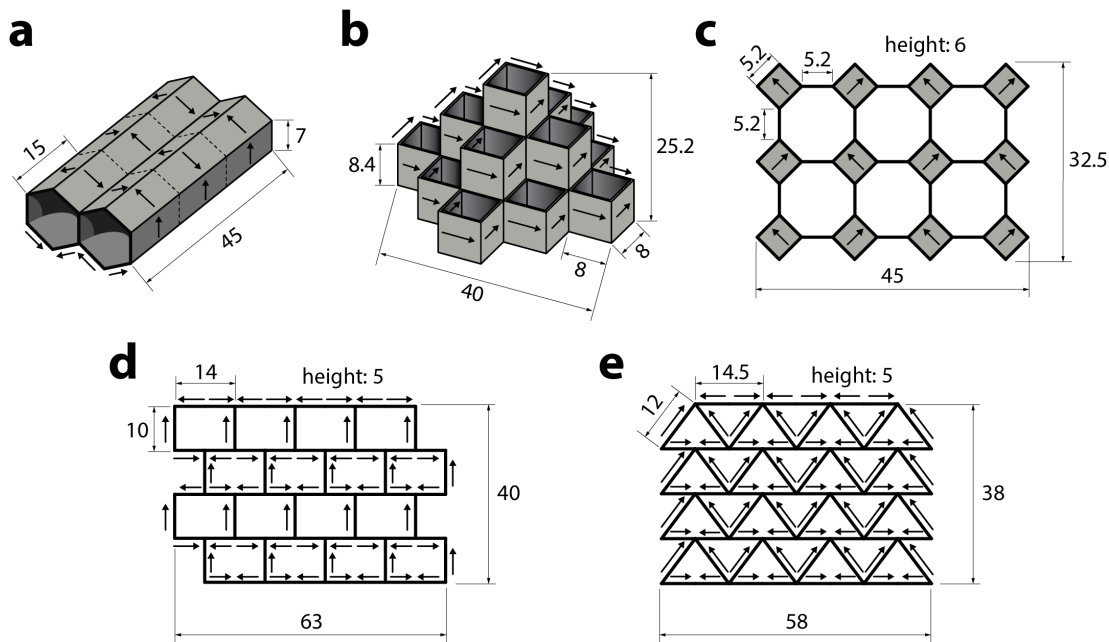


Fig. 2.18 | Schematic designs and dimensions of high-aspect-ratio multilayered structures. (a) Two adjoining hexagonal tubes programmed to form undulating surfaces under external magnetic fields; (b) a pyramid-shaped thin-walled structure programmed to elongate in its diagonal direction along the applied external fields; and (c-e) a set of auxetic structures with negative Poisson's ratios programmed to shrinkage in both length and width under external magnetic fields.

2.7 Materials and Methods

2.7.1 Ink Composition and Preparation

The magnetic ink was prepared first by blending two silicone-based materials - SE 1700 (Dow Corning Corp.) and Ecoflex 00-30 Part B (Smooth-on Inc.) - in a 1:2 volume ratio. Ecoflex 00-30 Part B, a softer elastomer than SE 1700, was used to achieve preferred mechanical properties of the composite material. Fumed silica nanoparticles (amorphous, 20-30 nm; US Research Nanomaterials Inc.), which corresponds to 12.5 wt% with respect to Ecoflex Part B, were added to achieve required rheological properties for direct ink writing. After mixing the blend in a planetary mixer (AR-100; Thinky) at 2,000 rpm for 2 min, 20 vol% NdFeB microparticles (287.5 wt% with respect to Ecoflex Part B) with an average size of 5 μm (MQFP-B-2007609-089; Magnequench) were added into the elastomer mixture and then mixed thoroughly at 2,000 rpm for

3 min, followed by defoaming at 2,200 rpm for 1 min. The composite ink was then magnetized by impulse magnetic fields (~ 2.7 T) generated by an impulse magnetizer (IM-10-30; ASC Scientific) to impart magnetic polarities to the ferromagnetic particles embedded in the elastomer matrix. Both SE 1700 and Ecoflex 00-30 are platinum-catalyzed, addition-curing silicones; hence, 10 wt% SE 1700 Catalyst with respect to SE 1700 Base was added into the magnetized ink and then mixed at 2,000 rpm for 30 s before printing. The final concentrations of components were as follows: 21.78 wt% Ecoflex 00-30 Part B, 2.72 wt% fumed silica nanoparticles, 11.71 wt% SE 1700 Base, 1.17 wt% SE 1700 Catalyst, and 62.62 wt% NdFeB microparticles. For imaging purpose, ~ 2 wt% fluorescent colorants (Ignite PMS 805C; Smooth-on Inc.) were added to this final composition.

The support ink, which was used for supporting structures when printing multilayered or 3D structures with the magnetic ink, was prepared by mixing a platinum-based silicone-curing accelerator (Elastosil CAT PT-F; Wacker) with fumed silica nanoparticles (amorphous, 20-30 nm; US Research Nanomaterials, Inc.) in a 5.45:1 mass ratio. Fumed silica nanoparticles were added to achieve rheological properties required for direct ink writing of the support ink. The higher concentration of catalyst in the support ink prevents diffusion of catalyst molecules from the adjacent magnetic inks, and therefore helps prevent imperfect curing of the printed magnetic structures. After the magnetic inks were fully cured upon heating at 120 °C for 1 hr, the fugitive support ink was removed by rinsing with isopropyl alcohol using an orbital shaker (Micro Plate Shaker; VWR).

2.7.2 Rheological Characterization

Rheological responses (Fig. 2.3) of the magnetic and support inks were characterized using a rotational rheometer (AR-G2; TA Instruments) with a 20-mm-diameter steel plate geometry. For magnetic inks, both magnetized and nonmagnetized samples were tested to evaluate the effects of magnetic interaction between the embedded magnetized particles. Apparent viscosities were measured via steady state flow experiments with a sweep of shear rates (0.01-100 s⁻¹). Shear storage moduli were measured as a function of shear stress via oscillation experiments at a fixed frequency of 1 Hz with a sweep of stress (10-10,000 Pa). The magnetic and support inks were equilibrated at 25 °C for 1 min before testing, and all experiments were performed at 25 °C with a gap height of 0.5 mm.

2.7.3 Magnetic Characterization

The quality of alignment of the magnetic particles was evaluated by measuring magnetic moment density (magnetization) of the printed samples with a vibrating sample magnetometer (DMS 1660; ADE Technologies) as shown in Fig. 2.6a. To prepare specimens, a set of parallel lines was printed in the same direction to construct a rectangular film. Then, the printed film was cut into circles using a 6-mm biopsy punch (Miltex Inc.) to fit into the sample holder of the machine. Magnetic moments of the samples were measured against a sweep of external magnetic fields from -8,000 to 8,000 A/m. Remanent magnetization, which corresponds to the measured magnetic moment when the applied external field is zero, was divided by each specimen's volume to obtain the magnetic moment density of the specimen.

2.7.4 Mechanical Characterization

The mechanical property of the printed elastomeric composite is required for model-based simulation, which will be discussed in the following chapter. For mechanical testing, two types of rectangular planar sheets (width: 12 mm; length: 35 mm) were printed with an 840- μm conical nozzle under no external magnetic field and PM-induced fields, respectively. After curing, the sheets were cut into dog-bone-shaped specimens with known dimensions (width: 4 mm; gauge length: 17 mm) for tensile testing. The cross-sectional area of each specimen was calculated by dividing the sample's original volume by its length, where the volume was calculated based on the sample's mass measured before the cut and the density (2.434 g/cm³) of the composite ink containing 20 vol% of NdFeB. The specimens were tested on a mechanical testing machine (Z2.5; Zwick/Roell) with a 20 N load cell at a strain rate of 0.01 s⁻¹. Nominal stress-stretch curves were plotted for both materials, and shear moduli (G) were obtained by fitting the experimental curves using a neo-Hookean model (Fig. 2.19). The obtained shear modulus of the magnetized-ink-based material was $G = 330$ kPa. The specimen printed in the presence of external fields showed higher shear modulus compared with the specimen printed without external fields ($G = 245$ kPa). This higher shear modulus may be attributed to the field-induced alignment of ferromagnetic particles along the filaments when magnetic fields were applied during the printing.

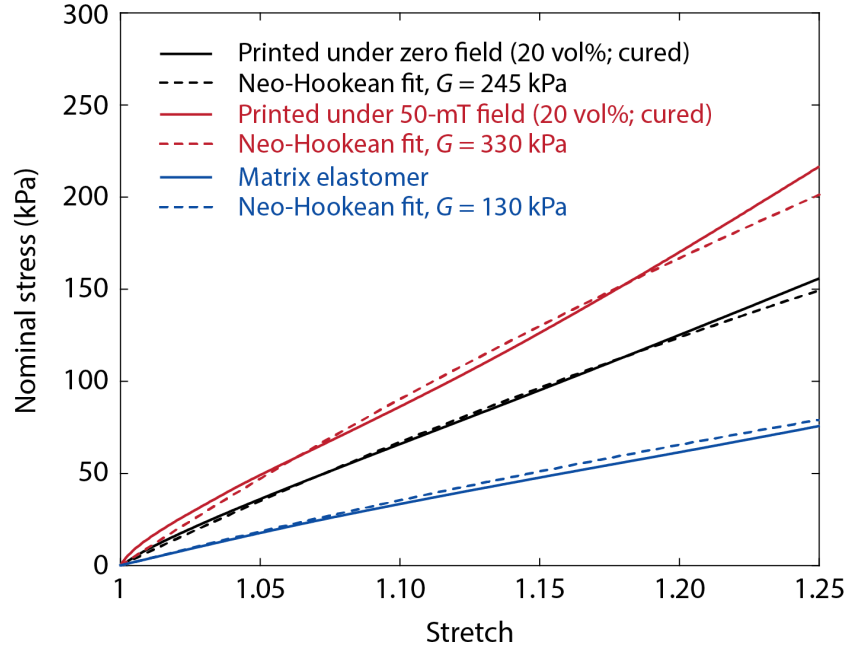


Fig. 2.19 | Mechanical responses of printed magnetic inks after curing. Nominal stress-stretch curves (solid lines) were obtained from uniaxial tensile tests of specimens printed with the magnetic ink in the absence of external fields (black) and under applied magnetic fields of 50 mT (red) at the nozzle tip generated by a permanent magnet. The elastomer matrix with no magnetic particles included was also tested (blue). Shear modulus (G) of each material was obtained by fitting the experimental curves using a neo-Hookean model (dashed lines).

3. MODELING OF HARD-MAGNETIC SOFT MATERIALS

3.1 Introduction

In this chapter, we develop a model to predict the transformation of complex 3D-printed structures under magnetic fields due to the programmed ferromagnetic domains resulting from the embedded hard-magnetic particles. Application of magnetic fields induces torques on the particles, which create stresses that collectively lead to a macroscale material response.

3.1.1 Magnetoactive Soft Materials

Magnetoactive soft materials, or magnetorheological elastomers, are commonly composed of polymeric matrices incorporating magnetic particles, typically iron or alloy of iron (26-30). Under applied magnetic fields, the embedded magnetic particles interact with each other and with the elastomer matrices to rapidly and dramatically change the mechanical properties such as stiffness or the shape in controlled manners (31). The controlled variations of mechanical properties in magnetoactive soft materials have been used in applications such as vibration absorbers (27, 32, 33), and isolators (34, 35). On the other hand, the controlled shape changes of magnetoactive soft materials have been explored for applications such as untethered soft actuators (36-38), biomimetic pumps (39), and drug-delivery devices (5, 40).

3.1.2 Soft-magnetic vs Hard-magnetic Materials

Despite their interesting properties and promising applications, existing magnetoactive soft materials have remained unable to create complex 3D shapes that might lead to complex functions for further realistic applications in many areas. One major limitation results from the fact that those existing magnetoactive materials are mostly based on soft-magnetic particles with low coercivity such as carbonyl iron or iron oxides (28, 41, 42), which develop strong magnetization when exposed to external magnetic fields but lose the induced magnetization quite easily when demagnetizing fields are applied. On the contrary, hard-magnetic materials such as NdFeB or SmCo (Samarium Cobalt) possess high coercivity, meaning that they can retain the remnant magnetization against relatively strong demagnetizing fields without significantly losing their magnetic polarities unlike the soft-magnetic materials.

The different magnetic properties of soft-magnetic and hard-magnetic materials are well illustrated by magnetization curves presented in Fig. 3.1 below. These curves show the hysteretic magnetic properties of each type of materials when exposed to an external magnetic field $\mathbf{H}^{\text{applied}}$. The magnetic hysteresis is one of the distinct properties of ferromagnetic materials. Other types of magnetic materials such as paramagnetic or diamagnetic materials exhibit no hysteretic properties. The M-H curves in Fig. 3.1a show how the magnetic moment densities of soft-magnetic and hard-magnetic materials change as the external applied field varies. Ferromagnetic materials typically develop strong magnetization due to their high permeabilities. The magnetization approaches a constant values, called saturation magnetization, as the magnetizing field increases. Once saturated, ferromagnetic materials maintain a remnant or residual magnetization, \mathbf{M}^r , even when the external applied fields are removed, which is the source of permanent magnetic polarities. The field strength at which the magnetization becomes zero is called intrinsic coercivity \mathbf{H}^{ci} . The field strength at which the magnetic flux density, denoted as \mathbf{B} in Fig. 3.1b, becomes zero is called coercivity or coercive force \mathbf{H}^c .

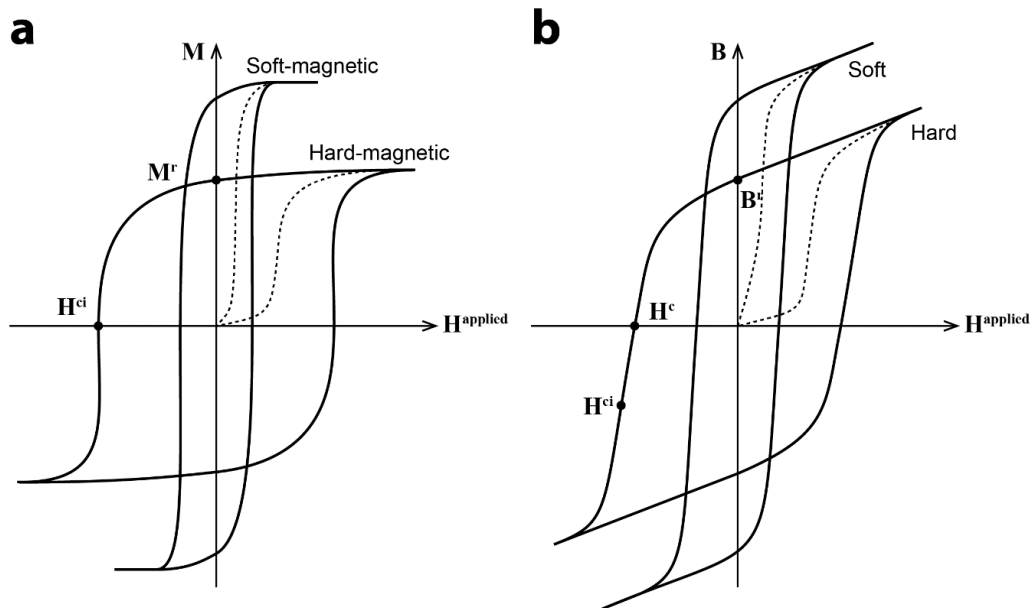


Fig. 3.1 | Magnetization characteristics of soft-magnetic and hard-magnetic materials. (a) Magnetization and (b) magnetic induction (flux density) developed in materials plotted against the applied external field.

For the proposed fabrication method introduced in Chapter 2 to work, the embedded ferromagnetic particles should be able to possess permanent magnetic polarities by retaining residual magnetization. Not only that, the embedded ferromagnetic materials should also possess coercivity high enough to resist demagnetization under external magnetic fields for actuation. When soft-magnetic materials are used, the programmed domains would be easily reverted by the applied actuation fields, which makes it difficult to achieve desired shapes in a controllable manner. For these reasons, hard-magnetic materials are preferred in our proposed fabrication method.

3.1.3 Model-guided Design of Complex Shape-morphing Structures

To design complex programmed shapes, thereby achieving functionally useful shape-morphing structures, the capability to quantitatively predict the programmed transformation is indispensable. For such a capability, a model based on constitutive relations to describe the physical behaviors of our materials is required. The capability to quantitatively predict how a designed structure will transform in response to different actuation fields enables designing multiple modes of programmed shape changes as shown in Fig. 3.2. Moreover, when guided by such model-based simulations, we can design previously inaccessible modes of transformation such as remotely controlled 3D auxetic behaviors, as already shown in the previous chapter.

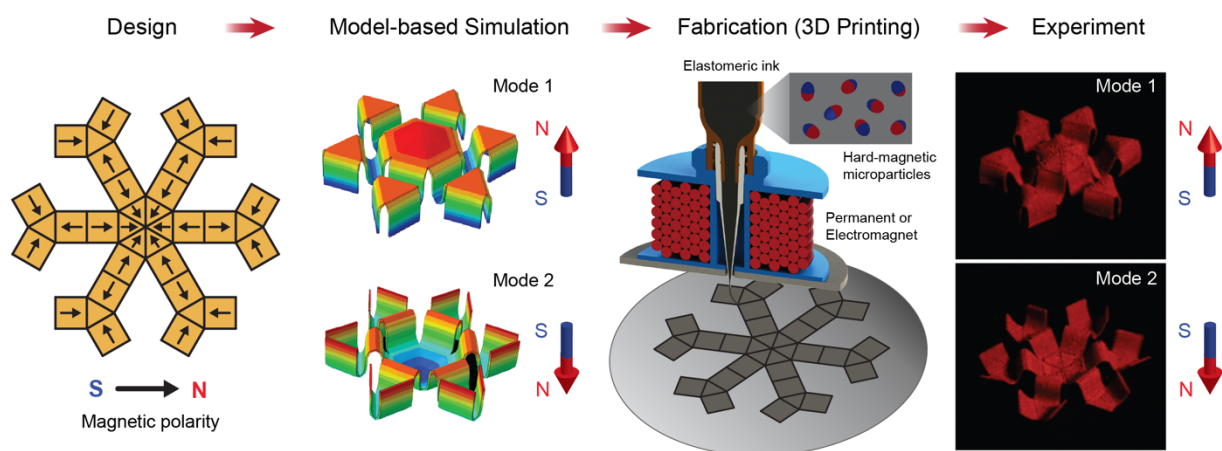


Fig. 3.2 | Model-guided design of printed shape-morphing structures. The model-based simulation can guide the design of complex shape-morphing structures based on the capability to predict multiple modes of transformation depending on the applied field directions.

3.2 Basic Equations

3.2.1 Kinematics

To discuss the basic kinematic relations, we first need to consider a deformable solid in a reference, undeformed state with material points specified by their position vectors \mathbf{X} . In a deformed state, the material points \mathbf{X} occupies the position $\mathbf{x} = \chi(\mathbf{X}, t)$, where $\chi(\mathbf{X}, t)$ denotes the motion of the body that maps the material points \mathbf{X} into \mathbf{x} . The deformation gradient tensor \mathbf{F} is defined by

$$\mathbf{F} = \text{Grad}\chi, \quad (3.1)$$

where Grad denotes the gradient operator with respect to \mathbf{X} with $J = \det \mathbf{F}$ denoting the volumetric Jacobian. The Cauchy stress tensor (the true stress tensor) and the Piola stress tensor (the nominal stress tensor) are denoted as $\boldsymbol{\sigma}$ and \mathbf{P} , respectively, whose relation is expressed as

$$\boldsymbol{\sigma} = \mathbf{P}\mathbf{F}^T / J \quad \text{or} \quad \mathbf{P} = J\boldsymbol{\sigma}\mathbf{F}^{-T}. \quad (3.2)$$

It should be noted that the stress tensors are the total stresses, which account for the both stress components: one from pure mechanical deformation and the other induced by magnetic fields in magnetoactive materials.

In what follows, we will express the magnetic field vector and the magnetic flux density vector in the material in the current configuration as \mathbf{H} and \mathbf{B} , respectively. Correspondingly, the magnetic field vector and the magnetic flux density vector in the reference configuration will be denoted as $\tilde{\mathbf{H}}$ and $\tilde{\mathbf{B}}$, respectively. Then, the relation between \mathbf{H} and $\tilde{\mathbf{H}}$ can be expressed as

$$\mathbf{H} = \mathbf{F}^{-T}\tilde{\mathbf{H}} \quad \text{or} \quad \tilde{\mathbf{H}} = \mathbf{F}^T\mathbf{H}. \quad (3.3)$$

Likewise, the relation between \mathbf{B} and $\tilde{\mathbf{B}}$ can be expressed as

$$\mathbf{B} = \mathbf{F}\tilde{\mathbf{B}} / J \quad \text{or} \quad \tilde{\mathbf{B}} = J\mathbf{F}^{-1}\mathbf{B}. \quad (3.4)$$

3.2.2 Equilibrium Equations

The conservation of mass for our continuum material requires the following relation to be satisfied:

$$\rho = \tilde{\rho} / J \quad \text{or} \quad \tilde{\rho} = \rho J, \quad (3.5)$$

where ρ is the mass density of the material in the current configuration and $\tilde{\rho}$ is the mass density of the material in the reference configuration.

Since we are interested in the shape changes of our printed structures under the applied magnetic fields, but not in the dynamics or time-varying shapes affected by inertial effects, we can safely assume that the accelerations of all material points are zero. Then, the equilibrium equation in the current configuration can be written in the following form:

$$\text{div } \boldsymbol{\sigma} + \mathbf{f} = \mathbf{0}, \quad (3.6)$$

where $\text{div } \boldsymbol{\sigma}$ denotes the divergence of $\boldsymbol{\sigma}$ with respect to \mathbf{x} , and \mathbf{f} denotes the body force per unit volume of the material in the current configuration. Correspondingly, the equilibrium equation in the reference configuration can be written in the following form:

$$\text{Div } \mathbf{P} + \tilde{\mathbf{f}} = \mathbf{0}, \quad (3.7)$$

where $\text{Div } \mathbf{P}$ denotes the divergence of \mathbf{P} with respect to \mathbf{X} , and $\tilde{\mathbf{f}}$ denotes the body force per unit volume of the material in the reference configuration. It should be noted that the body force here account for the gravitational force but not the magnetic force; the effect from magnetic interactions are considered in the stress tensors, which will be discussed in the following section. The relation between the body forces in the reference and current configurations is expressed as

$$\mathbf{f} = \tilde{\mathbf{f}} / J \quad \text{or} \quad \tilde{\mathbf{f}} = \mathbf{f} J. \quad (3.8)$$

Given that the free current and time-varying electric displacement are zero in our system, the Maxwell's equations in the current configuration can be expressed as

$$\text{div } \mathbf{B} = 0, \quad (3.9a)$$

$$\text{curl } \mathbf{H} = \mathbf{0}, \quad (3.9b)$$

where $\text{div} \mathbf{B}$ denotes the divergence of \mathbf{B} with respect to \mathbf{x} , and $\text{curl} \mathbf{H}$ denotes the curl of \mathbf{H} with respect to \mathbf{x} . Correspondingly, the Maxwell's equations in the reference configuration can be expressed as

$$\text{Div} \tilde{\mathbf{B}} = 0, \quad (3.10a)$$

$$\text{Curl} \tilde{\mathbf{H}} = \mathbf{0}, \quad (3.10b)$$

where $\text{Div} \tilde{\mathbf{B}}$ denotes the divergence of $\tilde{\mathbf{B}}$ with respect to \mathbf{X} , and $\text{Curl} \tilde{\mathbf{H}}$ denotes the curl of $\tilde{\mathbf{H}}$ with respect to \mathbf{X} .

3.2.3 Boundary Conditions

The mechanical boundary condition in the current configuration can be expressed as

$$[\boldsymbol{\sigma}] \mathbf{n} = \mathbf{0}, \quad (3.11)$$

where $[\]$ indicates a discontinuity of variable of interest across the surface, and \mathbf{n} denotes the outward unit normal vector with respect to the surface in the current configuration. Correspondingly, the mechanical boundary condition in the reference configuration can be expressed as

$$[\mathbf{P}] \mathbf{N} = \mathbf{0}, \quad (3.12)$$

where \mathbf{N} is the unit normal vector with respect to the surface in the reference configuration.

Given that the free current and the time-varying electric displacement is zero in the system, the magnetic boundary conditions in the current configuration can be expressed as

$$\mathbf{n} \cdot [\mathbf{B}] = 0, \quad (3.13a)$$

$$\mathbf{n} \times [\mathbf{H}] = \mathbf{0}, \quad (3.13b)$$

where \times denotes the cross product of two vectors. Correspondingly, the magnetic boundary conditions in the reference configuration can be expressed as

$$\mathbf{N} \cdot [\tilde{\mathbf{B}}] = 0, \quad (3.14a)$$

$$\mathbf{N} \times [\tilde{\mathbf{H}}] = \mathbf{0}. \quad (3.14b)$$

3.3 Constitutive Modeling

3.3.1 General Form of the Constitutive Relations

As discussed earlier, ferromagnetic materials can possess remnant magnetization once the materials are magnetized to saturation. This quantity corresponds to the magnetization that remains in the ferromagnetic material even after the applied external field is removed, creating permanent magnetic polarities of the material. In the current configuration, the residual magnetic flux density resulting from the remnant magnetization is defined as

$$\mathbf{B}^r = \mathbf{B} \Big|_{\mathbf{H}=0}. \quad (3.15)$$

Correspondingly, the residual magnetic flux density in the reference configuration is defined as

$$\tilde{\mathbf{B}}^r = \tilde{\mathbf{B}} \Big|_{\tilde{\mathbf{H}}=0}. \quad (3.16)$$

Then, from Eq. (3.4), the relation between \mathbf{B}^r and $\tilde{\mathbf{B}}^r$ can be expressed as

$$\mathbf{B}^r = \mathbf{F} \tilde{\mathbf{B}}^r / J \quad \text{or} \quad \tilde{\mathbf{B}}^r = \mathbf{J} \mathbf{F}^{-1} \mathbf{B}^r. \quad (3.17)$$

Following the convention in nonlinear elasticity and thermodynamics, we will define the constitutive model for our hard-magnetic soft materials based on the Helmholtz free energy function, \tilde{W} , which denotes the Helmholtz free energy per unit volume of the material in the reference configuration. The Helmholtz free energy function \tilde{W} is considered as a function of two independent variables — the deformation gradient \mathbf{F} and the magnetic flux density $\tilde{\mathbf{B}}$ — with one state variable $\tilde{\mathbf{B}}^r$ which denotes the residual magnetic flux density in the reference configuration. In a mathematical expression, this statement can be written as $\tilde{W}(\mathbf{F}, \tilde{\mathbf{B}})$. From the energy balance and work-conjugate relationship (readers may consult (43) for detailed derivations)

for hyperelastic materials, we can arrive the following expressions that relate the Piola stress and the magnetic field vector, both expressed in the current configuration, with the Helmholtz free energy, the deformation gradient, and the magnetic flux density:

$$\mathbf{P} = \frac{\partial \tilde{W}(\mathbf{F}, \tilde{\mathbf{B}})}{\partial \mathbf{F}}, \quad (3.18a)$$

$$\tilde{\mathbf{H}} = \frac{\partial \tilde{W}(\mathbf{F}, \tilde{\mathbf{B}})}{\partial \tilde{\mathbf{B}}}. \quad (3.18b)$$

Substituting the above equations to Eqs. (3.2) and (3.3) further leads to the following expressions in terms of both variables written in the reference configuration:

$$\boldsymbol{\sigma} = \frac{1}{J} \frac{\partial \tilde{W}(\mathbf{F}, \tilde{\mathbf{B}})}{\partial \mathbf{F}} \mathbf{F}^T, \quad (3.19a)$$

$$\mathbf{H} = \mathbf{F}^{-T} \frac{\partial \tilde{W}(\mathbf{F}, \tilde{\mathbf{B}})}{\partial \tilde{\mathbf{B}}}. \quad (3.19b)$$

Application of magnetic fields to our hard-magnetic soft materials induces torques on the embedded ferromagnetic particles, making them reoriented towards the applied external field. These magnetic torques create internal stresses that collectively lead to a macroscale material response, causing the whole structure to transform into a configuration that minimizes the combined magnetic and elastic potential energy of the system. This discussion will be further elaborated in the following sections.

3.3.2 Ideal Hard-magnetic Soft Materials

The Helmholtz free energy can be divided into two parts: i) the elastic part $\tilde{W}^{\text{elastic}}(\mathbf{F})$, also called as strain energy density which is a function of the deformation gradient \mathbf{F} only, and ii) the magnetic part $\tilde{W}^{\text{magnetic}}(\mathbf{F}, \tilde{\mathbf{B}})$, or magnetic potential energy density, as a function of both the deformation gradient \mathbf{F} and the nominal magnetic flux density $\tilde{\mathbf{B}}$ with the state variable $\tilde{\mathbf{B}}^r$. The

elastic part can be one of the following models which are most commonly used to describe constitutive laws for soft materials: neo-Hookean, Gent (44), and Arruda-Boyce (45) models.

To describe the magnetic part of the Helmholtz free energy, we propose a model called *ideal hard-magnetic soft material* which is depicted in Fig. 3.3. This model assumes that, in a hard-magnetic soft material in the current configuration, the magnetic field \mathbf{H} is linearly related to the magnetic flux density induced by the magnetic field $\mathbf{B} - \mathbf{B}^r$ by a constant permeability over a certain range within which the applied magnetic field strength is lower than the coercivity of the embedded ferromagnetic materials. When the applied magnetic field approaches or exceeds the coercivity \mathbf{H}^c , however, which means outside the working range beyond which the linear relationship is no longer valid, the $\mathbf{B} - \mathbf{H}$ curve becomes nonlinear and follows the hysteresis loop illustrated in Fig. 3.3a. Considering the fact that the required field strength to actuate our printed structures based on elastomer matrix incorporating NdFeB particles, i.e. 200 mT which corresponds to 160 kA/m, is far lower than the coercivity of the NdFeB particles, which is 490 kA/m, it is reasonable to assume that the aforementioned linear relationship holds true for our model described in Fig. 3.3b.

The reasoning behind such a linear approximation comes from the fact that the permeability of ferromagnetic materials after being saturated is close to that of the surrounding media. In our case of considering an elastomer matrix with embedded hard-magnetic particles, we can further point out the fact that the permeability of silicone rubber is almost the same as vacuum permeability which is often denoted as μ_0 . Such reasoning leads to a conclusion that the permeability of our hard-magnetic soft materials can be approximated as the vacuum permeability μ_0 provided that the materials are fully magnetized to saturation during the ink preparation. In a mathematical expression, this linear constitutive model can be written as

$$\mathbf{H} = \frac{1}{\mu_0} (\mathbf{B} - \mathbf{B}^r). \quad (3.20a)$$

This expression is valid for the sample's residual induction \mathbf{B}^r aligned with the applied external field \mathbf{H} . It should be noted, however, that this linear relation holds true even when the printed sample's residual induction \mathbf{B}^r is not in line with the applied external field \mathbf{H} . When the residual

induction vector \mathbf{B}^r is decomposed into components along (\mathbf{B}_{\parallel}^r) and perpendicular (\mathbf{B}_{\perp}^r) to the applied field direction, the aforementioned linear relation needs to be modified as the following form:

$$\mathbf{H} = \frac{1}{\mu_0} (\mathbf{B} - \mathbf{B}_{\parallel}^r). \quad (3.20b)$$

It is worth noting that this relation also implies the statement that the remnant magnetization \mathbf{M}^r and thus the residual induction \mathbf{B}^r can be considered to be independent of the applied external field as long as the field strength does not exceed the limit of coercivity.

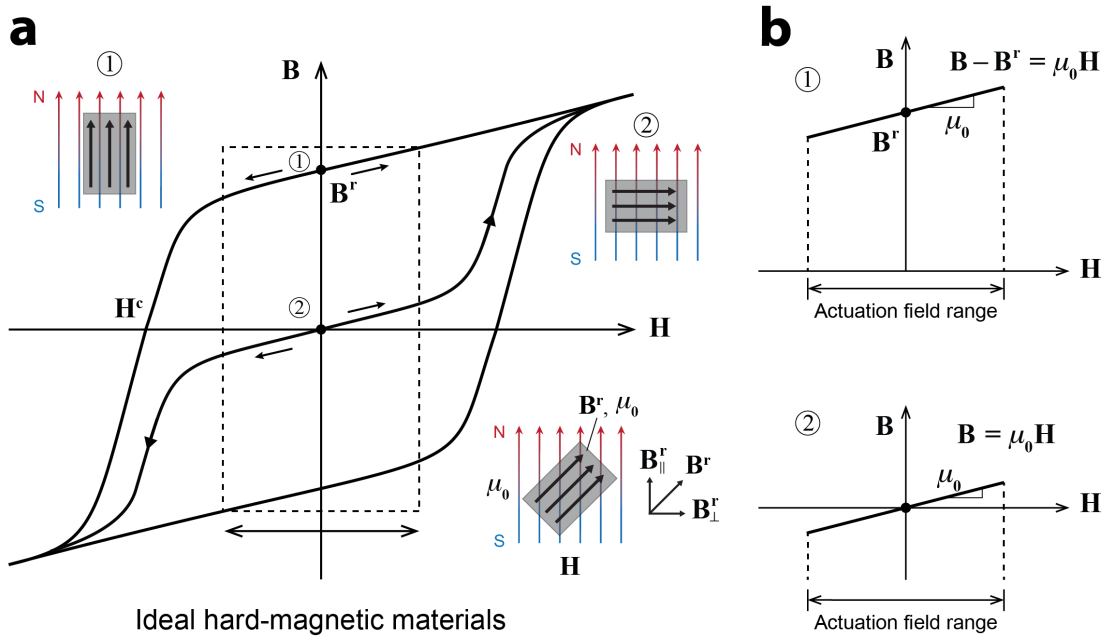


Fig. 3.3 | Ideal hard-magnetic soft materials characterized by a linear B - H relationship. (a) A hysteresis loop of typical hard-magnetic materials. (b) The linear relationship between \mathbf{B} and \mathbf{H} within the actuation field range below the coercivity \mathbf{H}^c . In the model of ideal hard-magnetic soft materials, this linear relationship is assumed to hold true even when the residual induction \mathbf{B}^r is not aligned with the applied external field \mathbf{H} ; only the offset \mathbf{B}_{\parallel}^r at which the \mathbf{B} - \mathbf{H} curve meets the y -axis varies depending on the angle θ between \mathbf{B}^r and \mathbf{H} while the linear relation is maintained.

3.3.3 Specific Form of the Constitutive Relations

The fact that our hard-magnetic soft materials, when magnetically saturated, have the permeability almost the same as the vacuum permeability has an important implication necessary to evaluate the magnetic potential energy, from which we will obtain the magnetic Cauchy stress tensors. Since the whole material composed of an elastomer matrix with embedded hard-magnetic particles is considered to have the vacuum permeability, we can safely assume that the presence of our hard-magnetic soft materials will not significantly alter the applied magnetic field. Then, when a uniform magnetic field $\mathbf{B}^{\text{applied}}$ is applied to the hard-magnetic soft material with remnant magnetization $\mathbf{M}^r = \mathbf{B}^r / \mu_0$, the magnetic potential energy per unit volume in the current state can be expressed as

$$W^{\text{magnetic}} = -\frac{1}{\mu_0} \mathbf{B}^r \cdot \mathbf{B}^{\text{applied}}, \quad (3.21)$$

when neglecting the higher order terms. Then, given that $\tilde{W}^{\text{magnetic}} = W^{\text{magnetic}} J$ and Eq. (3.17), the magnetic potential energy in the reference configuration can be expressed as

$$\tilde{W}^{\text{magnetic}} = -\frac{1}{\mu_0} \mathbf{F} \tilde{\mathbf{B}}^r \cdot \mathbf{B}^{\text{applied}}. \quad (3.22)$$

Assuming the generalized neo-Hookean solid for our elastomeric composite material, the strain energy density, or the elastic potential energy per unit volume of the reference (undeformed) body can be expressed as

$$\tilde{W}^{\text{elastic}}(\mathbf{F}) = \frac{G}{2} (J^{-2/3} I_1 - 3) + \frac{K}{2} (J - 1)^2, \quad (3.23)$$

where G and K are the material's shear modulus and bulk modulus, respectively, and I_1 is the first principal invariant defined as $I_1 = \text{tr}(\mathbf{F}\mathbf{F}^T)$ with \mathbf{F} representing the deformation gradient tensor, which characterizes local length changes in the elastic body. The quantity J , the volumetric Jacobian of the deformation, is defined as $J = \det \mathbf{F}$ and characterizes the local volume changes. For incompressible solid, the deformation must satisfy $J = 1$ to preserve volume. It should be noted that, as discussed earlier, the specific form of this elastic part of the Helmholtz free energy

can be other models such as Gent or Arruda-Boyce. In this thesis, given that the maximum strain level is modest, and hence, that the chain-locking or stiffening behavior can be neglected, the neo-Hookean model would provide sufficient accuracy in terms of predicting the final shape, especially when considering the fact that the mechanical testing results are fitted well with this simple model.

The combined Helmholtz free energy of the our hard-magnetic soft material can then be expressed as

$$\tilde{W} = \frac{G}{2} \left(J^{-2/3} I_1 - 3 \right) + \frac{K}{2} (J-1)^2 - \frac{1}{\mu_0} \mathbf{F} \tilde{\mathbf{B}}^r \cdot \mathbf{B}^{\text{applied}}. \quad (3.24)$$

From the general constitutive relations in Eqs. (3.18) and (3.19), we derive can obtain the elastic Piola and Cauchy stresses as

$$\mathbf{P}^{\text{elastic}} = GJ^{-2/3} \left(\mathbf{F} - \frac{I_1}{3} \mathbf{F}^{-T} \right) + KJ(J-1) \mathbf{F}^{-T}, \quad (3.25a)$$

$$\boldsymbol{\sigma}^{\text{elastic}} = GJ^{-5/3} \left(\mathbf{F} \mathbf{F}^T - \frac{I_1}{3} \mathbf{I} \right) + K(J-1) \mathbf{I}, \quad (3.25b)$$

respectively, where \mathbf{I} denotes the identity tensor. Likewise, the magnetic Piola and Cauchy stresses can be calculated as

$$\mathbf{P}^{\text{magnetic}} = -\frac{1}{\mu_0} \mathbf{B}^{\text{applied}} \otimes \tilde{\mathbf{B}}^r, \quad (3.26a)$$

$$\boldsymbol{\sigma}^{\text{magnetic}} = -\frac{1}{\mu_0 J} \mathbf{B}^{\text{applied}} \otimes \mathbf{F} \tilde{\mathbf{B}}^r, \quad (3.26b)$$

respectively, where the operator \otimes denotes the dyadic product, which takes two vectors to yield a second order tensor. The magnetic Cauchy stress can be further expressed in terms of true (instead of nominal) quantities as

$$\boldsymbol{\sigma}^{\text{magnetic}} = -\frac{1}{\mu_0} \mathbf{B}^{\text{applied}} \otimes \mathbf{B}^r, \quad (3.27)$$

Finally, we obtain the total Cauchy stress tensor as

$$\boldsymbol{\sigma} = GJ^{-5/3} \left(\mathbf{F} \mathbf{F}^T - \frac{I_1}{3} \mathbf{I} \right) + K(J-1) \mathbf{I} - \frac{1}{\mu_0 J} \mathbf{B}^{\text{applied}} \otimes \mathbf{F} \tilde{\mathbf{B}}^r. \quad (3.28)$$

Since $\mathbf{B}^{\text{applied}}$ and $\tilde{\mathbf{B}}^r$ are given, the Cauchy stress tensor $\boldsymbol{\sigma}$ is a function of the deformation gradient \mathbf{F} only. By substituting the Cauchy stress tensor into the equilibrium equation Eq. (3.6), one can calculate the deformation gradient \mathbf{F} in the hard-magnetic soft material.

3.4 Scaling Analysis of Simple Magnetic Actuation

For quantitative understanding of the effects of physical parameters on the magnetic actuation of our printed samples, we analyze the bending of a beam with a uniform magnetic domain under applied field. Let us consider a rectangular beam with one end clamped as depicted in Fig. 3.4. The length, thickness, and width of the beam are denoted as L , H , and W , respectively, and the cross-sectional area and the volume of the beam are denoted as A and V , respectively. The beam is considered to have uniform magnetization of magnitude M along the axial direction and is subject to a uniform field of strength B , which is being applied perpendicularly to the beam.

Assuming a small deflection of the beam, the curvature of the deformed beam can be expressed as

$$\kappa(x) = \frac{\tau(x)}{EI}, \quad (3.29)$$

where E denotes the Young's modulus of the beam. For incompressible material, E can be calculated from the material's shear modulus μ , which gives $E = 3G$. The area moment of inertia I is defined as $I = AH^2 / 12$. In addition, the torque density $d\tau$, which is induced by the applied magnetic field, can be calculated as $d\tau = MBdV = MBA dx$. Thereafter, the torque applied at a distance x from the fixed end can be calculated as

$$\tau(x) = MBA(L - x). \quad (3.30)$$

From Eq. (3.29), the curvature can then be expressed as a function of x as

$$\kappa(x) = \frac{4MB(L - x)}{GH^2}. \quad (3.31)$$

From this equation, we can notice that the maximum curvature, which occurs at the base ($x = 0$), scales as

$$\kappa_{\max} \propto \frac{MBL}{GH^2}. \quad (3.32)$$

We can infer from this expression that there are a number of strategies to achieve effective actuation that yields large curvature. A more straightforward approach is to increase either the magnetization strength M or the actuation field B . The magnetization strength can be increased by either increasing the volume fraction of ferromagnetic microparticles or by increasing the applied field strength during the printing process to achieve better quality of alignment. Another strategy is to increase the length-to-area ratio (L / H^2) by printing more slender fibers to construct a shape-morphing structure. The last strategy is to reduce the material's shear modulus G , which can be achieved by reducing the crosslinking density of the elastomer matrix of the composite ink.

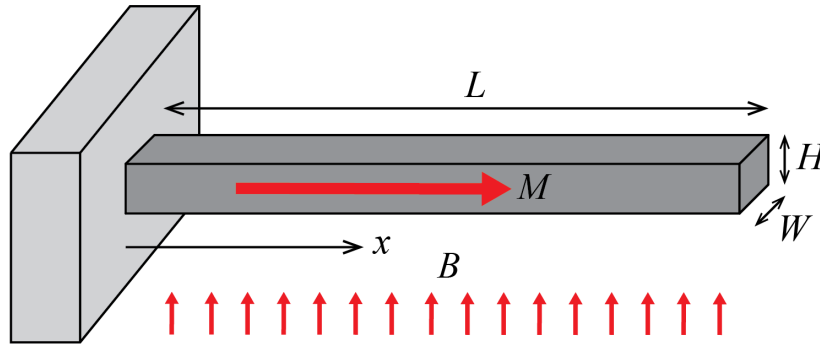


Fig. 3.4 | A schematic model for scaling analysis of magnetic actuation of a simple beam. The length, thickness, and width of the beam are denoted as L , H , and W , respectively, and the cross-sectional area and the volume of the beam are denoted as A and V , respectively. The beam is considered to have uniform magnetization of magnitude M along the axial direction and is subject to a uniform external field of strength B , which is being applied perpendicularly to the beam.

3.5 Validation of the Computational Model

3.5.1 Simulation Results vs Analytical Solutions

The constitutive relation in Eq. (3.28), which is developed to compute the magnetic-stress-induced deformation, is implemented as a user-defined element (UEL) subroutine in the commercial FEA software ABAQUS for model-based simulation. For validation of the implemented model, the following two simple cases are considered: when the applied external field $\mathbf{B}^{\text{applied}}$ is 1) parallel and 2) perpendicular to the magnetization $\tilde{\mathbf{B}}^r / \mu_0$ possessed by the solid body. For case 1), the UEL-based simulation results were obtained in terms of stretch λ and compared with analytical values calculated from the constitutive relation in Eq. (3.28). For case 2), beams in bending (for small deflections) due to the magnetic torques were considered and the UEL-based simulation results were obtained in terms of beam deflections at given $\tilde{\mathbf{B}}^r / \mu_0$ and $\mathbf{B}^{\text{applied}}$. These values were compared with the calculated deflection values under mechanical loads that create bending moments equivalent to the magnetic torques.

1) When $\mathbf{B}^{\text{applied}}$ is parallel with $\tilde{\mathbf{B}}^r$

Assume that both $\mathbf{B}^{\text{applied}}$ and $\tilde{\mathbf{B}}^r$ are aligned with the 1-direction in the reference configuration. When $\mathbf{B}^{\text{applied}}$ and $\tilde{\mathbf{B}}^r$ are parallel, the magnetic interaction results in uniaxial loading, which is described by the deformation gradient tensor in the form of

$$[\mathbf{F}] = \begin{bmatrix} \lambda & 0 & 0 \\ 0 & \lambda^{-1/2} & 0 \\ 0 & 0 & \lambda^{-1/2} \end{bmatrix}, \quad (3.33)$$

where λ denotes the stretch along the loading direction. The elastic term of the Cauchy stress along the uniaxial loading direction can be calculated from Eq. (3.25b) as

$$\sigma_{11}^{\text{elastic}} = GJ^{-5/3}(\lambda^2 - \lambda^{-1}) + K(J - 1), \quad (3.34)$$

while the other terms satisfy $\sigma_{22}^{\text{elastic}} = \sigma_{22}^{\text{elastic}} = 0$ due to the traction-free condition on the lateral sides. From Eq. (3.26b), the magnetic Cauchy stress term in the deformed body is calculated as

$$\sigma_{11}^{\text{magnetic}} = -\frac{1}{\mu_0 J} \lambda \tilde{\mathbf{B}}^r B^{\text{applied}}. \quad (3.35)$$

To reach equilibrium, this magnetic Cauchy stress should be balanced by the elastic stress term. Given that the elastomeric material of interest can be regarded as incompressible solid, which satisfies $J=1$, we can then obtain a following dimensionless quantity by balancing Eqs. (3.33) and (3.35) as

$$\frac{\tilde{\mathbf{B}}^r B^{\text{applied}}}{\mu_0 G} = \lambda - \frac{1}{\lambda^2}. \quad (3.36)$$

The dimensionless quantity $G^{-1} \mu_0^{-1} \tilde{\mathbf{B}}^r B^{\text{applied}}$ as a function of the stretch λ is plotted as a solid line in Fig. 3.5a. The case when $G^{-1} \mu_0^{-1} \tilde{\mathbf{B}}^r B^{\text{applied}} = 0$ corresponds to the undeformed reference configuration in which no magnetic interaction is involved. When $\mathbf{B}^{\text{applied}}$ and $\tilde{\mathbf{B}}^r$ are in the same direction ($G^{-1} \mu_0^{-1} \tilde{\mathbf{B}}^r B^{\text{applied}} > 0$), the magnetic stress term contributes to a uniaxial elongation of the body ($\lambda > 1$) along the direction of the applied external field. When $\mathbf{B}^{\text{applied}}$ and $\tilde{\mathbf{B}}^r$ are in the opposite direction, a compressive stress develops, causing the body to shrink ($\lambda < 1$) along the applied field direction. The finite element simulation results obtained for several values of $G^{-1} \mu_0^{-1} \tilde{\mathbf{B}}^r B^{\text{applied}}$ are plotted as red circles in Fig. 3.5a. These simulation results faithfully follow the analytical prediction (black line) given in Eq. (3.36), validating that the implemented model is working correctly in the case of parallel $\mathbf{B}^{\text{applied}}$ and $\tilde{\mathbf{B}}^r$.

2) When $\mathbf{B}^{\text{applied}}$ is perpendicular to $\tilde{\mathbf{B}}^r$

To validate the UEL-based simulation results when $\mathbf{B}^{\text{applied}}$ is being applied perpendicularly to $\tilde{\mathbf{B}}^r$, a simple case of beam bending with small deflection is evaluated. More specifically, a slender, incompressible solid beam (length L) with a rectangular cross section (width W and height $H = L/10$), whose one end is rigidly fixed, is considered to have uniform magnetization

$\tilde{\mathbf{B}}^r$ along the axial 1-direction under a uniform external field $\mathbf{B}^{\text{applied}}$ along the 2-direction that is perpendicular to the beam (Fig. 3.4). The magnetic torque induces a small deflection of the beam as the embedded magnetic dipoles in line with $\tilde{\mathbf{B}}^r$ attempt to align themselves with the applied $\mathbf{B}^{\text{applied}}$ field. In the reference configuration, namely $\mathbf{F} = \mathbf{I}$, the only non-zero term of the magnetic Cauchy stress in the incompressible body is calculated as $\sigma_{21}^{\text{magnetic}} = -\mu_0^{-1} \tilde{B}^r B^{\text{applied}}$ from Eq. (3.26b). This shear stress gives rise to the magnetic torque $\tau = \mu_0^{-1} \tilde{B}^r B^{\text{applied}} LWH$ across the entire beam.

Now, let us consider a point load P acting on the free end of the beam in the reference configuration. The point load required to produce an equivalent bending moment as τ can be calculated as $P = \mu_0^{-1} \tilde{B}^r B^{\text{applied}} WH$. Then, the deflection of the free end of the beam, or the maximal deflection δ_{max} , under the point load P can be expressed in a dimensionless form as

$$\frac{\delta_{\text{max}}}{L} = \frac{4\tilde{B}^r B^{\text{applied}} L^2}{3G\mu_0 H^2}, \quad (3.37)$$

for small deflections ($\delta_{\text{max}} / L < 10\%$), which forms a linear relation with the dimensionless quantity $G^{-1} \mu_0^{-1} \tilde{B}^r B^{\text{applied}}$ as plotted as a black line in Fig. 3.5b. For some prescribed values of this dimensionless quantity, the deflection values were obtained from the simulation based on finite-element model and plotted as red squares in Fig. 3.5b. The two results show good agreement, suggesting that the implemented model is working correctly in the case when $\mathbf{B}^{\text{applied}}$ and $\tilde{\mathbf{B}}^r$ are orthogonal.

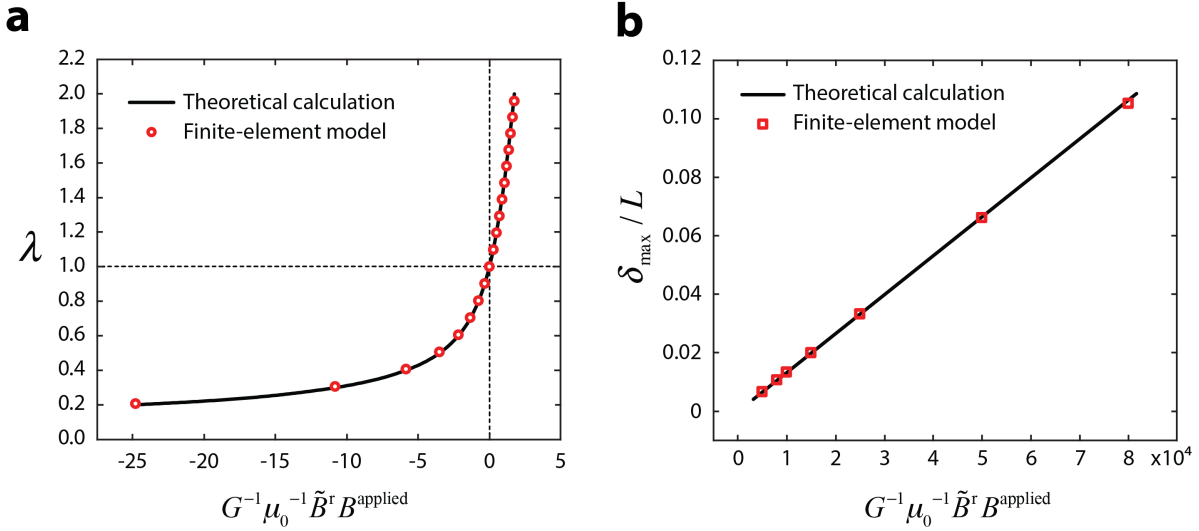


Fig. 3.5 | Comparison of the simulations results with analytical solutions. (a) Comparison of magnetic-stress-induced stretch λ as a function of dimensionless quantity $G^{-1}\mu_0^{-1}\tilde{\mathbf{B}}^r \mathbf{B}^{\text{applied}}$, when external magnetic field $\mathbf{B}^{\text{applied}}$ is parallel with the residual induction $\tilde{\mathbf{B}}^r$ (b) Comparison of small deflections at the free end of a slender beam when $\mathbf{B}^{\text{applied}}$ is applied perpendicularly to $\tilde{\mathbf{B}}^r$ in order to create magnetic-torque-induced bending.

3.5.2 Experimental Validation

In Chapter 2, we have already discussed a variety of printed structures with designed ferromagnetic domains and thus programmed shape changes. From the very illustrative 1D example to complex 3D shapes, we compared the experimental results with the simulation results that were obtained from our finite-element model discussed throughout this chapter. All of the examples presented in Figs. 2.5, 2.9-11, and 2.16-17 showed good agreement between the experimental and simulation results, which validates the developed computational model. As a summary, we choose some complex 2D and 3D shapes and compare their experimental and simulation results by overlaying the two images as shown in Fig. 3.6.

The overlaid images show that the final deformed shapes of the presented structures are very close to the shapes predicted by the finite element simulation. We reason that the slight difference between the experimental and simulation results of the hollow cross structure shown in Fig. 3.6a is attributed to the fact that the experiment was performed under a non-uniform field

generated by a single permanent magnet due to the limited size of the available electromagnet. However, the simulation assumed a uniform magnetic field for actuation of the hollow cross structure. Application of such a gradient magnetic field might have contributed to an attractive magnetic force acting on the printed structure, thereby resulting a slightly less prominent shape when compared with what predicted by the finite element simulation. However, given that other overlaid images show very good agreement, we can conclude the our computational model is valid and accurate enough to guide the design of complex shape morphing structures based on our 3D printing platform capable of programming ferromagnetic domains in soft materials.

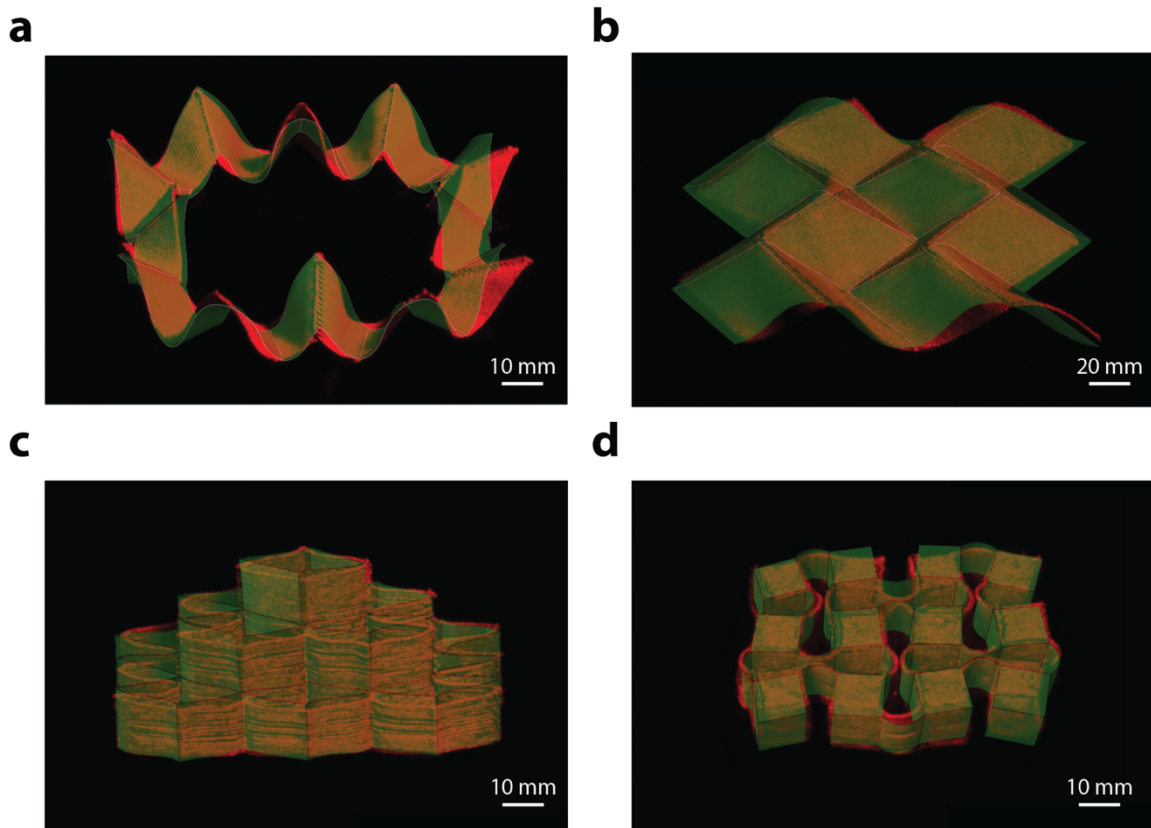


Fig. 3.6 | Experimental validation of finite-element simulations of 2D and 3D structures. All demonstrated structures were printed with the magnetic ink containing 20 vol% of NdFeB particles through a nozzle with diameter of 410 μm under the applied field of 50 mT at the nozzle tip generated by a permanent magnet. Magnetic actuation was performed by applying external fields of 200 mT generated by a permanent magnet for (a) and (d) and by a pair of electromagnets for (c) and (d).

4. APPLICATIONS OF PRINTED MAGNETIC SHAPE SHIFTERS

4.1 Actuation Performance of Printed Shape-shifting Structures

In the design and fabrication of shape-programmable soft materials, intensive efforts have been made to increase the level of complexity by adopting 3D printing techniques such as inkjet printing (46), stereolithography (47, 48), and direct ink writing (49). However, fast and fully reversible actuation between programmed shapes has remained a central challenge in the field. To quantitatively evaluate the actuation performance, we compare the energy density and the actuation rate of printed shape-programmable materials in the literature. We also compare the power density, which is one of the most widely used metric to evaluate the actuation performance of active materials. The comparison shows that both the energy and power densities of our printed soft materials with programmed ferromagnetic domains are orders of magnitude higher than those of other existing 3D-printed soft active materials.

4.1.1 Energy and Power Densities

In an undeformed state, where no deformation exists, the elastic potential energy of the structure is minimum. When an external magnetic field is applied, for example, perpendicularly to the magnetic domains, the magnetic potential energy is maximum at the instant. When neglecting the hysteretic energy dissipation that results from the Mullin's effect (50), which is commonly observed in elastomers filled with particulate materials, the magnetic potential energy is converted to elastic potential energy as the structure deforms. In the final state, as a result, the magnetic potential energy is minimum while the elastic potential energy is maximum, but the total combined potential energy should be minimum because it is energetically preferable. In what follows, we will see that this qualitative argument is more or less a true statement supported by quantitative measurements and calculations as well.

Although the exact value of the elastic potential energy should be obtained from stress-strain, which is not perfectly linear, the elastic potential energy per unit volume, ρ_E [J/m³], can be approximated under the assumptions of linear elasticity and incompressibility as

$$\rho_E \simeq \frac{3}{2} G \epsilon_a^2, \quad (4.1)$$

where G [Pa] is the shear modulus of the composite material, and ε_a is the actuation strain developed in the deformed state under the applied magnetic fields. On the other hand, the magnetic potential energy density, ρ_M [J/m³], can be approximated as

$$\rho_M \approx MB, \quad (4.2)$$

where M and B denotes the magnetization value and the applied field strength, respectively. It should be noted that this expression is valid when the external magnetic field \mathbf{B} is applied perpendicularly to the magnetization vector \mathbf{M} of the printed structure.

The energy density is the quantity that denotes the amount of energy stored in the material due to its elasticity upon deformation as a result of the mechanical work done on the material. Then, the power density, ρ_w , which is essentially the amount of mechanical power extracted from the actuation of the material, can be obtained simply by multiplying the actuation rate or frequency f [Hz] to the energy density. Our shape-morphing structures discussed in Chapter 2 deform up to strain levels from 0.15 to 0.25. Given that the shear modulus measured from mechanical testing is $G = 330$ kPa, the elastic potential energy density is ranging from 11.13 to 30.93 kJ/m³. Also, given that the measured magnetization value is 78 kA/m and the actuation field strength is 200 to 400 mT, the calculated magnetic potential energy density is ranging from 15.6 to 31.2 kJ/m³. Considering the fact that the calculated elastic and magnetic potential energy densities are close to each other, we can deduce that the previous qualitative argument at the beginning of this section is valid. Given that our shape-morphing structures deform into final states within 0.1 to 0.5 s, the calculated power density is ranging from 22.3 to 309.3 kW/m³.

4.1.2 Comparison with Existing 3D-printed Soft Active Materials

In this section, we compare the actuation performance of our printed structures, which is evaluated by the energy and power densities discussed in the previous section, with those of existing 3D-printed soft active materials based on shape memory polymers, liquid crystal elastomers, swelling hydrogels, and so on. The energy density and actuation rate are compared in Fig. 4.1a, and the power density is compared in Fig. 4.1b. which are orders of magnitude greater than the actuation rates and power densities achieved by existing 3D-printed shape-transforming soft materials.

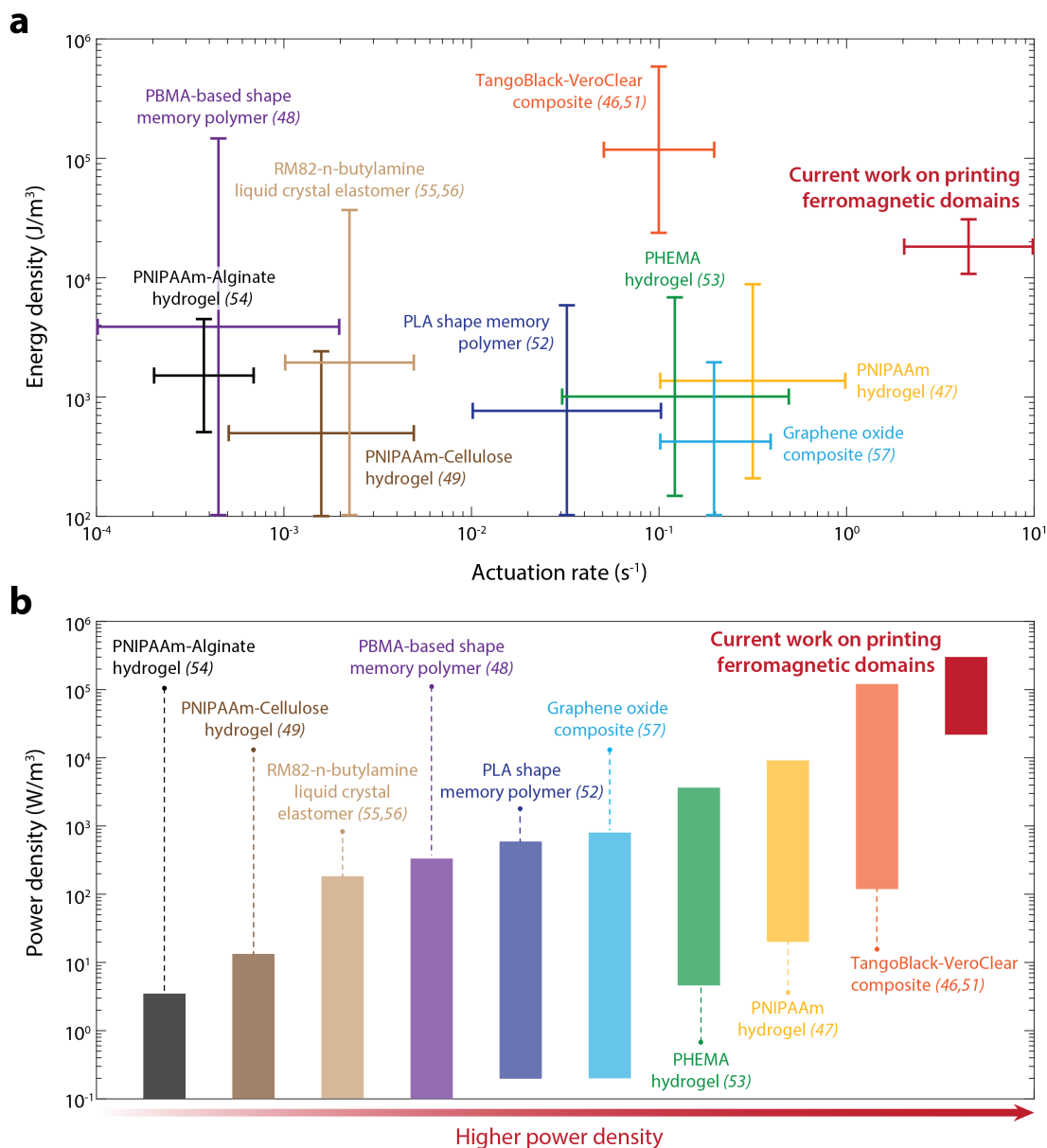


Fig. 4.1 | Actuation performance of 3D-printed shape-programmable soft materials. (a) Energy density and actuation rate of our magnetically responsive structures presented in Chapter 2 are plotted and compared with those of existing 3D-printed shape-programmable soft materials in the literature. (b) Power density is calculated as energy density multiplied by the actuation rate of each material and plotted for comparison; the materials are listed in order of increasing power densities. PNIPAAm = poly(N-isopropylacrylamide); PMBA = poly(benzyl methacrylate); PHEMA = poly(hydroxyl ethyl methacrylate); PLA = poly(lactic acid); RM82 = 1,4-bis-[4-(6-acryloyloxyhexyloxy)benzoyloxy]-2-methylbenzene.

4.2 Functions and Applications from Programmed Shape Changes

4.2.1 Reconfigurable Soft Electronics

The capability to create complex shape changes allows us to achieve diverse functions from our printed structures. First, by combining electronic components and circuitry with our annular ring structure in Fig. 2.9c, we print a soft electronic device as detailed in Fig. 4.2 below. This soft electronic device deforms into two different shapes depending on the direction of applied magnetic fields of 30 mT, and each mode of transformation yields a different electronic function (Fig. 4.3a and b): red micro-LEDs lit up in Mode 1 and green micro-LEDs lit up in Mode 2. This results demonstrate that our multimaterial 3D printing method could be used to design and fabricate functionally reconfigurable soft electronic devices, whose rigid-material counterparts have recently been achieved by means of multistable buckling (58). Fig. 4.3c shows a schematic diagram of the embedded soft electronic circuits, which are designed to turn active only in the designated mode of transformation due to the selective contact with the gold electrode on the substrate.

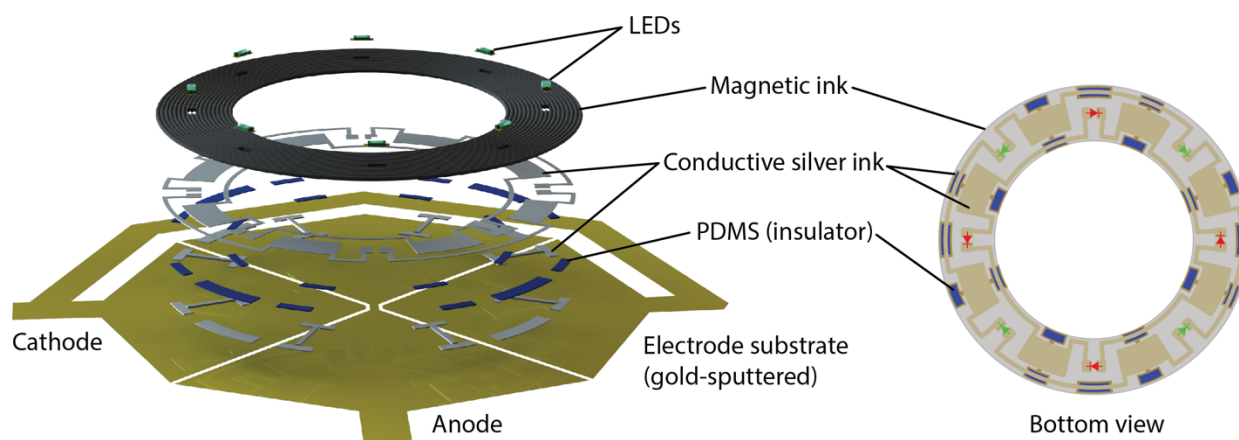


Fig. 4.2 | Exploded and bottom views of the reconfigurable soft electronic device. Soft electronic circuitry and components are embedded by means of a hybrid fabrication process based on multimaterial 3D printing.

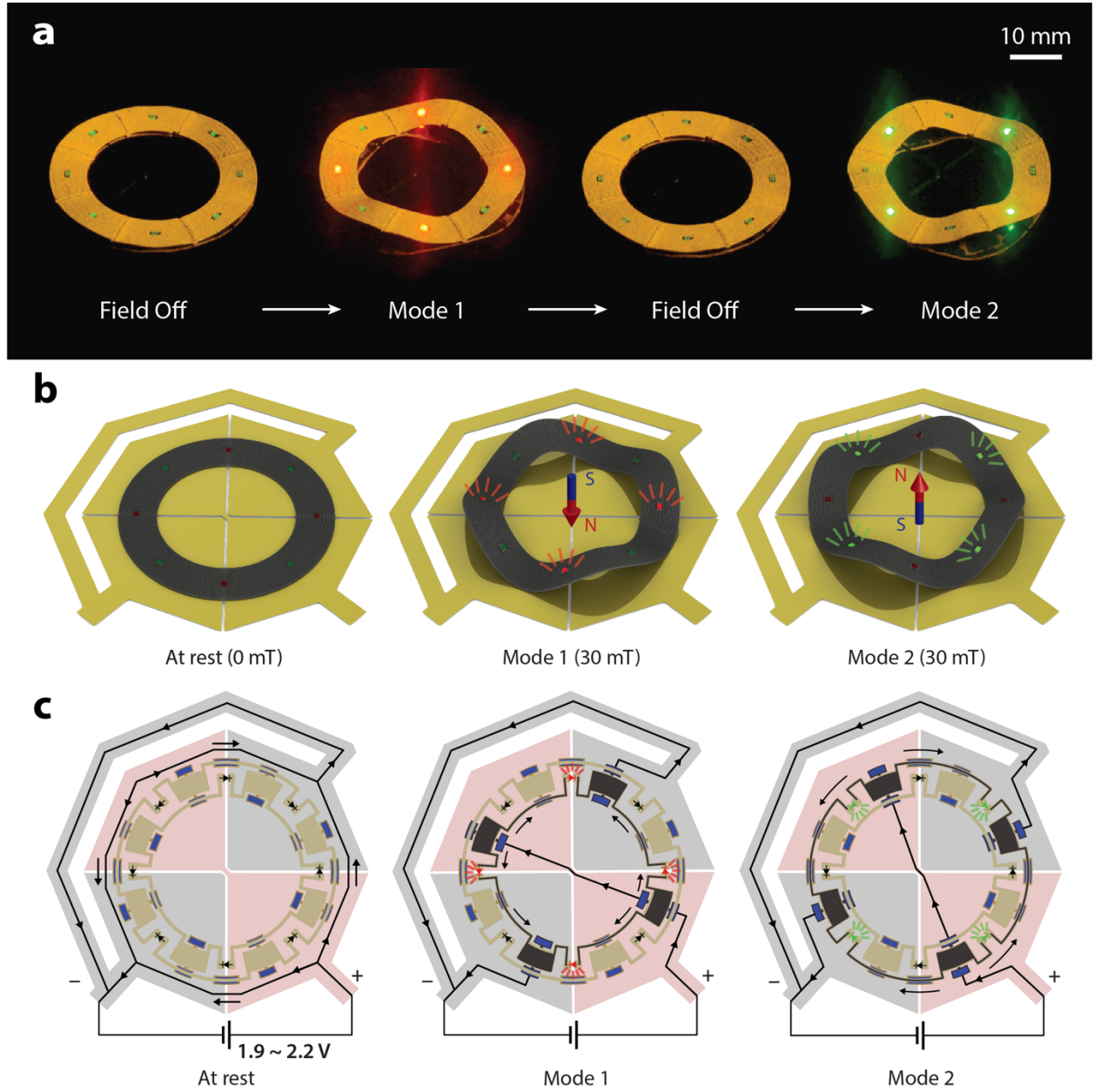


Fig. 4.3 | Demonstration and mechanism of the reconfigurable soft electronic device. (a, b) Two different shapes depending on the direction of applied magnetic fields of 30 mT, which yield different electronic functions (red micro-LEDs lit up in Mode 1 and green micro-LEDs lit up in Mode 2). (c) Schematic diagram of the embedded soft electronic circuits, which are designed to turn active only in the designated mode of transformation due to the selective contact with the golden electrode substrate.

4.2.2 Interaction with Fast-moving Objects

We further demonstrate the capability of interacting with an object based on the complex shape changes of the hexapedal structure shown in Fig. 2.11i. Using the fast response upon magnetic actuation, the hexapedal structure quickly stops a fast-moving object (Fig. 4.4c). When applying a magnetic field in the opposite direction to create a reversed shape (Fig. 3.1), the hexapedal structure can catch a falling object (Fig. 4.4a), hold it against external disturbance, and release the object on demand by using the previous mode of transformation (Fig. 4.4b). These series of tasks demonstrate that the printed shape-morphing structure is strong and agile enough to catch, hold, and lift the glass ball (with diameter of 18 mm and weight of 8 g), which is 10 times heavier than the hexapedal structure. These functional demonstrations suggest many new possibilities and applications in areas of soft robotics, especially where such untethered fast response and interaction with external objects are required.

4.2.3 Rolling-based Locomotion and Delivery of Drug Pills

Moreover, owing to the intricate patterns of ferromagnetic domains, which are enabled by the flexible fabrication method based on 3D printing, more complex behaviors can be created and thus more sophisticated functions can be derived from such complex shape changes. The hexapedal structure wraps its body and rotates along a horizontal axis under a rotating magnetic field (200 mT) generated by a permanent magnet. This coupled motion creates rolling-based locomotion, which allows the hexapedal structure to move forward and backward depending on the rolling direction as shown in Fig. 4.5. Harnessing the shape changes and motion, the hexapedal structure can carry an object with arbitrary shape such as a round (Fig. 4.6a) or oblong drug pill (Fig. 4.6b) and release the drug pill on demand as shown in Fig. 4.6. All such functions can be achieved by remotely controlling the applied magnetic fields without the need of direct mechanical contact. These demonstrations, along with the demonstrations above, show that a single structure encoded with intricate patterns of ferromagnetic domains can exhibit multiple modes of transformation depending on the applied field direction and strength, further implying many new possibilities in magnetically controlled and actuated soft robotic applications.

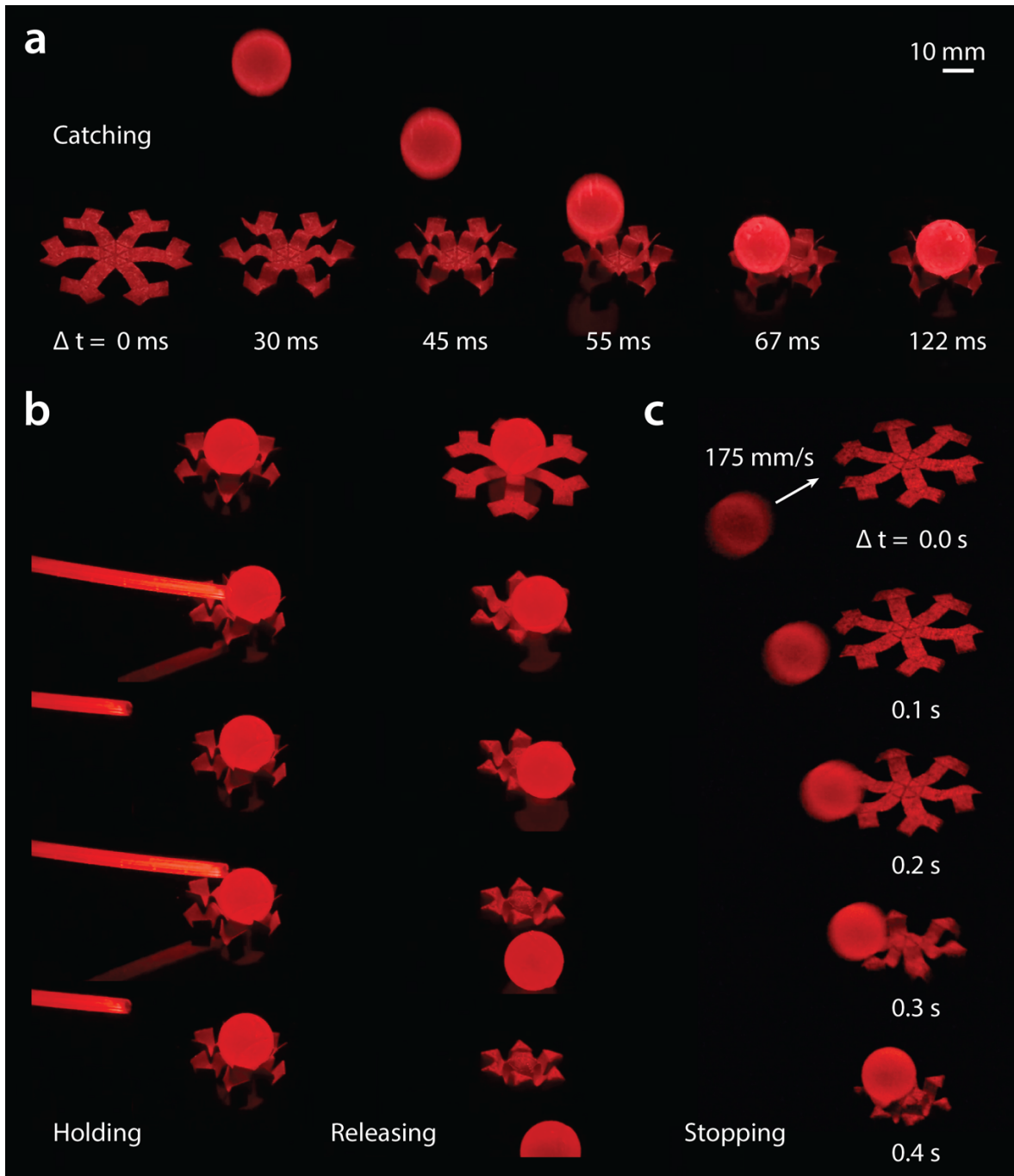


Fig. 4.4 | Demonstration of multiple functions of the printed hexapedal structure. (a) The hexapedal structure catching a glass ball (diameter 18 mm; weight 8 g) off the center using its second mode of transformation upon application of a magnetic field (200 mT) generated by a permanent magnet. (b) After catching the ball, the hexapedal structure holds the object against physical disturbance and releases the ball using the first mode of transformation. (c) The hexapedal structure can also stop a fast-moving glass ball.

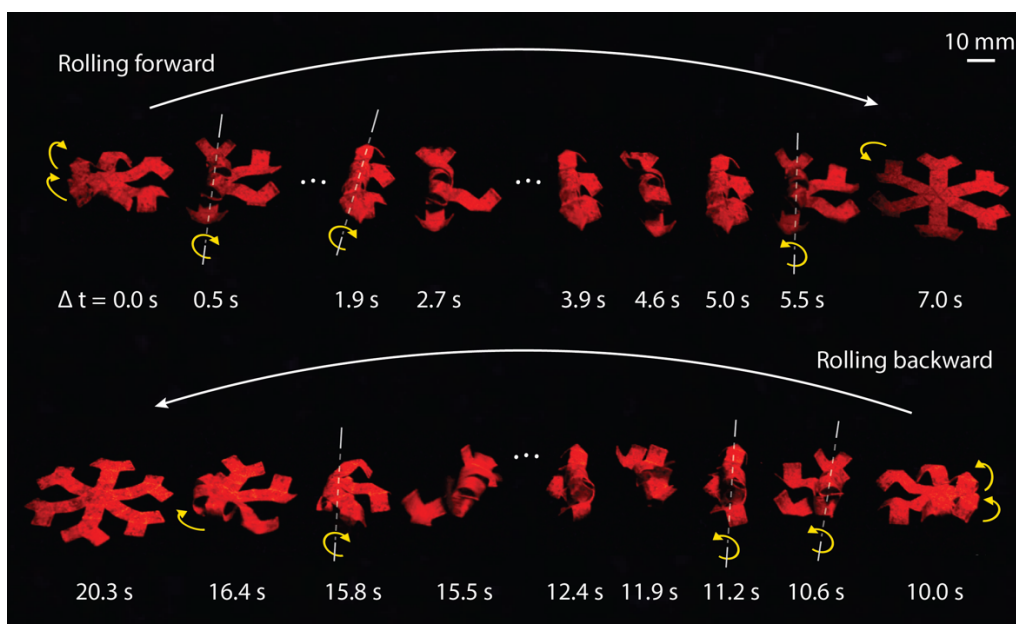


Fig. 4.5 | Demonstration of rolling-based locomotion of the printed hexapedal structure. The hexapedal structure wraps its body and rotates along a horizontal axis under a rotating magnetic field, moving forward and backward depending on the rolling direction.

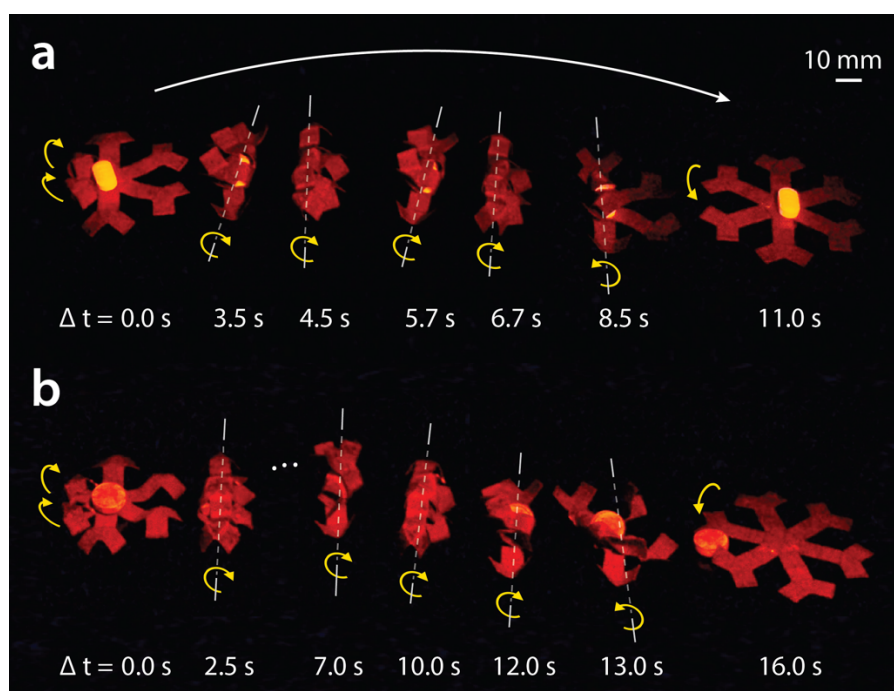


Fig. 4.6 | Rolling-based delivery of a pharmaceutical dose. (a) An oblong and (b) a round drug pill is carried by the hexapedal structure which wraps up the object and rolls forward under the applied rotating magnetic fields.

4.2.4 Horizontal Leap of 3D Auxetic Structure

The 3D mechanical metamaterial presented in Fig. 2.16c can show a horizontal leap based on the drastic release of the elastic and magnetic potential energy (Fig. 4.7). The fast response of the auxetic structure generates an average speed of 250 mm/s during the leap, allowing it to move forward by 120 mm within 0.7 seconds on the horizontal plane. This leaping motion is achieved by first applying a magnetic field in one direction to collapse the auxetic structure and then switching to a field in the opposite direction while attenuating the field strength. This sudden reversal of the field direction quickly increases the magnetic potential energy and triggers the drastic release of the stored elastic and magnetic potential energy, which is converted to kinetic energy during the horizontal leap. The detailed information on applying the magnetic fields for actuation is given in Fig. 4.8.

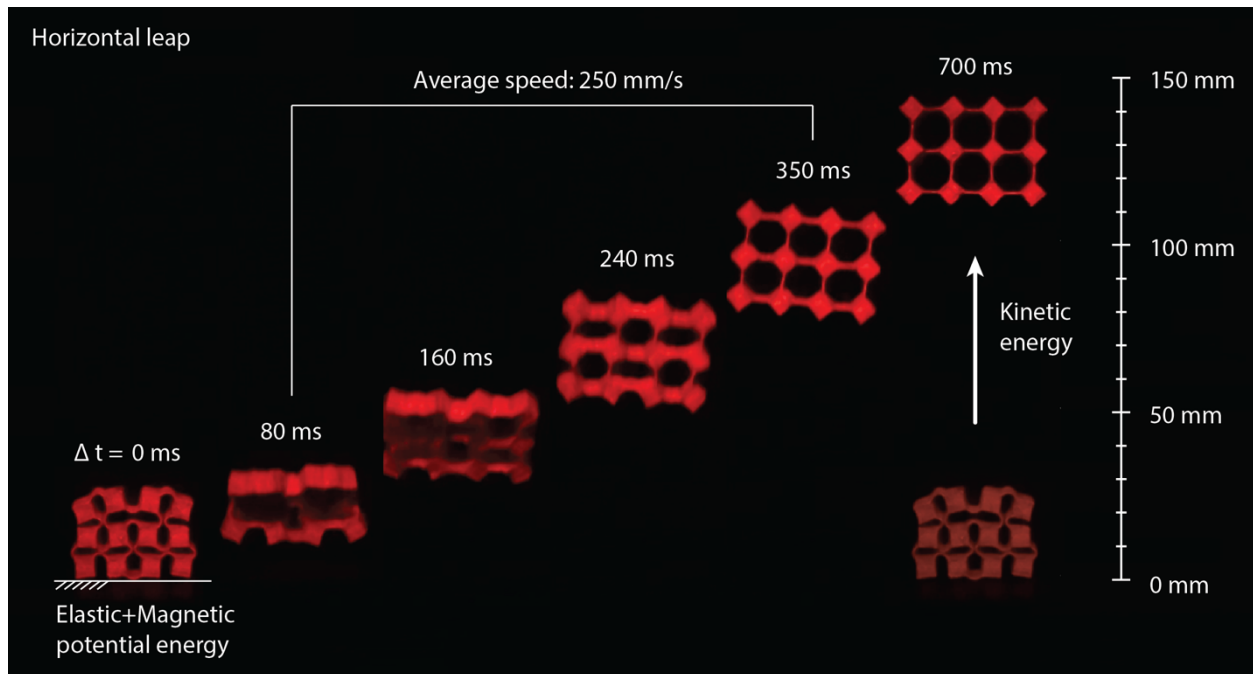


Fig. 4.7 | Horizontal leap of a 3D auxetic structure. The 3D auxetic structure shows leaping motion upon sudden reversal of the applied magnetic field direction while attenuating the strength by rotating a permanent magnet by 90 degrees.

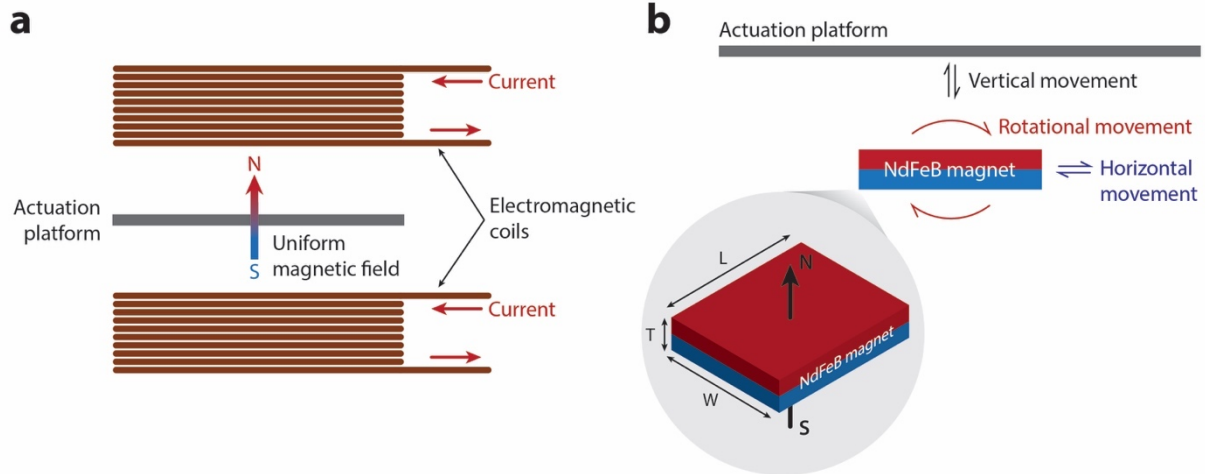


Fig. 4.8 | Methods of applying magnetic fields to actuate the printed structures. The magnetic fields for actuating the printed structures can be applied in two ways. (a) A pair of electromagnetic coils are used to generate a uniform magnetic field. (b) A NdFeB magnet (width: 2 inch; length: 3 inch; thickness: 0.5 inch; surface flux density: 300 mT) is used to create spatially varying magnetic fields for dynamic actuation by combining vertical, horizontal and rotational movements of the magnet.

5. CONCLUSIONS

This thesis aimed to deliver a detailed information about the mechanism, modeling, and applications of the proposed method of printing ferromagnetic domains in soft materials. In Chapter 2, we discussed a various examples of 2D and 3D structures which exhibit fast and fully reversible transformation into complex programmed shapes upon application of magnetic fields. We also discussed the key parameters in the printing process that were identified by experimental characterizations and analytical interpretations.

In Chapter 3, we developed a mathematical model based on a continuum mechanics framework, which enabled us to quantitatively predict the complex prograded shape changes resulting from the magnetic-torque-induced deformation. We also validated our developed model by comparing the simulation results with analytical solutions for simplified problems and also with experimental results for all of the demonstrated printed samples. The nice agreement between the simulation and experimental results verified that our developed model was valid and accurate enough to be able to guide the design of complex shape morphing structures produced by our proposed fabrication method.

In Chapter 4, we quantitatively evaluated the actuation performance of our printed shape-morphing structures including the energy density and the power density, which were orders of magnitude higher than those of existing 3D-printed active materials based on hydrogels, shape memory polymers, and liquid crystal elastomers. We also demonstrated diverse functions derived from multiple modes of transformation depending on the direction and strength of the applied actuation fields. From the series of functional demonstrations, we could conclude that our printed shape-shifting structures were strong and agile enough to be able to interact with fast-moving objects or environments via magnetic actuation, suggesting many new possibilities in the field of magnetically actuated and controlled soft robots.

Our printing method as a fabrication platform can be extended to multiple composite inks using different types of elastomer and hydrogel matrices and magnetic particles. The proposed method of printing ferromagnetic domains in soft materials introduces new design parameters including the domain patterns, magnetization strength, and actuation fields into the design and fabrication of shape-programmable soft materials. The remote actuation of such untethered, complex, and fast shape-shifting soft materials based on magnetic fields suggests new possibilities for applications in flexible electronics, biomedical devices, soft robotics, and so on.

6. REFERENCES

1. M. Ma, L. Guo, D. G. Anderson, R. Langer, Bio-inspired polymer composite actuator and generator driven by water gradients. *Science* **339**, 186-189 (2013).
2. M. Zarek *et al.*, 3D printing of shape memory polymers for flexible electronic devices. *Adv. Mater.* **28**, 4449-4454 (2016).
3. M. Wehner *et al.*, An integrated design and fabrication strategy for entirely soft, autonomous robots. *Nature* **536**, 451-455 (2016).
4. S. J. Park *et al.*, Phototactic guidance of a tissue-engineered soft-robotic ray. *Science* **353**, 158-162 (2016).
5. X. Zhao *et al.*, Active scaffolds for on-demand drug and cell delivery. *Proc. Natl Acad. Sci. USA* **108**, 67-72 (2011).
6. S. Fusco *et al.*, An integrated microrobotic platform for on-demand, targeted therapeutic interventions. *Adv. Mater.* **26**, 952-957 (2014).
7. K. A. Davis, K. A. Burke, P. T. Mather, J. H. Henderson, Dynamic cell behavior on shape memory polymer substrates. *Biomaterials* **32**, 2285-2293 (2011).
8. R. M. Erb, J. J. Martin, R. Soheilian, C. Pan, J. R. Barber, Actuating soft matter with magnetic torque. *Adv. Funct. Mater.* **26**, 3859-3880 (2016).
9. L. Hines, K. Petersen, G. Z. Lum, M. Sitti, Soft actuators for small-scale robotics. *Adv. Mater.* **29**, 1603483 (2017).
10. J. Rahmer, C. Stehning, B. Gleich, Spatially selective remote magnetic actuation of identical helical micromachines. *Science Robotics* **2**, eaal2845 (2017).
11. S. Martel, Beyond imaging: Macro-and microscale medical robots actuated by clinical MRI scanners. *Science Robotics* **2**, eaam8119 (2017).
12. M. Boncheva *et al.*, Magnetic self-assembly of three-dimensional surfaces from planar sheets. *Proc. Natl Acad. Sci. USA* **102**, 3924-3929 (2005).
13. J. Kim, S. Chung, S. Choi, H. Lee, S. Kwon, Programming magnetic anisotropy in polymeric microactuators. *Nat. Mater.* **10**, 747-752 (2011).
14. G. Z. Lum *et al.*, Shape-programmable magnetic soft matter. *Proc. Natl Acad. Sci. USA* **113**, E6007-E6015 (2016).
15. W. Hu, G. Z. Lum, M. Mastrangeli, M. Sitti, Small-scale soft-bodied robot with multimodal locomotion. *Nature* **554**, 81 (2018).
16. J. A. Lewis, Direct ink writing of 3D functional materials. *Adv. Funct. Mater.* **16**, 2193-2204 (2006).
17. J. L. Silverberg *et al.*, Using origami design principles to fold reprogrammable mechanical metamaterials. *Science* **345**, 647-650 (2014).
18. C. Yuan *et al.*, 3D printed reversible shape changing soft actuators assisted by liquid crystal elastomers. *Soft Matter*, (2017).
19. T. H. Ware, M. E. McConney, J. J. Wie, V. P. Tondiglia, T. J. White, Voxelated liquid crystal elastomers. *Science* **347**, 982-984 (2015).
20. A. Oyefusi, J. Chen, Reprogrammable chemical 3D shaping for origami, kirigami, and reconfigurable molding. *Angew. Chem.* **129**, 8362-8365 (2017).
21. Z. Zhao *et al.*, Origami by frontal photopolymerization. *Sci. Adv.* **3**, e1602326 (2017).
22. J. H. Na *et al.*, Programming reversibly self-folding origami with micropatterned photocrosslinkable polymer trilayers. *Adv. Mater.* **27**, 79-85 (2015).

23. S. Xu *et al.*, Assembly of micro/nanomaterials into complex, three-dimensional architectures by compressive buckling. *Science* **347**, 154-159 (2015).
24. Y. Zhang *et al.*, A mechanically driven form of kirigami as a route to 3D mesostructures in micro/nanomembranes. *Proc. Natl Acad. Sci. USA* **112**, 11757-11764 (2015).
25. S. Babaei *et al.*, 3D soft metamaterials with negative Poisson's ratio. *Adv. Mater.* **25**, 5044-5049 (2013).
26. J. M. Ginder, M. E. Nichols, L. D. Elie, J. L. Tardiff, Magnetorheological elastomers: properties and applications, in *Smart Structures and Materials 1999: Smart Materials Technologies* **3675**, 131-139 (1999).
27. Y. Li, J. Li, W. Li, H. Du, A state-of-the-art review on magnetorheological elastomer devices. *Smart Mater. Struct.* **23**, 123001 (2014).
28. Z. Rigbi, L. Jilken, The response of an elastomer filled with soft ferrite to mechanical and magnetic influences. *J. Magn. Magn. Mater.* **37**, 267-276 (1983).
29. M. R. Jolly, J. D. Carlson, B. C. Munoz, A model of the behaviour of magnetorheological materials. *Smart Mater. Struct.* **5**, 607 (1996).
30. J. Ginder, Rheology controlled by magnetic fields. *Encycl. Appl. Phys.* **16**, 487-503 (1996).
31. J. Ginder, S. Clark, W. Schlotter, M. Nichols, Magnetorheological phenomena in magnetorheological elastomers, in *Electrorheological Fluids and Magnetorheological Suspensions*, 472-478 (2002).
32. J. M. Ginder, W. F. Schlotter, M. E. Nichols, Magnetorheological elastomer in tunable vibration absorbers, in *Smart Structures and Materials 2001: Damping and Isolation*, **4331**, 103-111 (2001).
33. H. Deng, X. Gong, L. Wang, Development of an adaptive tuned vibration absorber with magnetorheological elastomer. *Smart Mater. Struct.* **15**, N111-N116 (2006).
34. S. Opie, W. Yim, Design and control of a real-time variable modulus vibration isolator. *J. Intell. Mater. Syst. Struct.* **22**, 113-125 (2011).
35. G. Liao, X. Gong, S. Xuan, C. Kang, L. Zong, Development of a real-time tunable stiffness and damping vibration isolator based on magnetorheological elastomer. *J. Intell. Mater. Syst. Struct.* **23**, 25-33 (2012).
36. S. Kashima, F. Miyasaka, K. Hirata, Novel soft actuator using magnetorheological elastomer. *IEEE Trans. Magn.* **48**, 1649-1652 (2012).
37. H. Böse, R. Rabindranath, J. Ehrlich, Soft magnetorheological elastomers as new actuators for valves. *J. Intell. Mater. Syst. Struct.* **23**, 989-994 (2012).
38. V. Q. Nguyen, R. Ramanujan, Novel coiling behavior in magnet-polymer composites. *Macromol. Chem. Phys.* **211**, 618-626 (2010).
39. S. Hong *et al.*, Magnetoactive sponges for dynamic control of microfluidic flow patterns in microphysiological systems. *Lab Chip* **14**, 514-521 (2014).
40. C. A. Cezar *et al.*, Biphasic ferrogels for triggered drug and cell delivery. *Adv. Health. Mater.* **3**, 1869-1876 (2014).
41. M. Zrínyi, L. Barsi, A. Büki, Deformation of ferrogels induced by nonuniform magnetic fields. *J. Chem. Phys.* **104**, 8750-8756 (1996).
42. L. Borcea, O. Bruno, On the magneto-elastic properties of elastomer-ferromagnet composites. *J. Mech. Phys. Solids* **49**, 2877-2919 (2001).
43. L. Dorfmann, R. W. Ogden, *Nonlinear Theory of Electroelastic and Magnetoelastic Interactions*. Springer US, (2016).
44. A. Gent, A new constitutive relation for rubber. *Rubber Chem. Technol.* **69**, 59-61 (1996).

45. E. M. Arruda, M. C. Boyce, A three-dimensional constitutive model for the large stretch behavior of rubber elastic materials. *J. Mech. Phys. Solids* **41**, 389-412 (1993).
46. Z. Ding *et al.*, Direct 4D printing via active composite materials. *Sci. Adv.* **3**, e1602890 (2017).
47. J. Kim, J. A. Hanna, M. Byun, C. D. Santangelo, R. C. Hayward, Designing responsive buckled surfaces by halftone gel lithography. *Science* **335**, 1201-1205 (2012).
48. Q. Ge *et al.*, Multimaterial 4D printing with tailorable shape memory polymers. *Sci. Rep.* **6**, 31110 (2016).
49. A. S. Gladman, E. A. Matsumoto, R. G. Nuzzo, L. Mahadevan, J. A. Lewis, Biomimetic 4D printing. *Nat. Mater.* **15**, 413-418 (2016).
50. R. W. Ogden, D. G. Roxburgh, A pseudo-elastic model for the Mullins effect in filled rubber. *Proc. R. Soc. Lond. A. Math. Phys. Sci.* **455**, 2861-2877 (1999).
51. J. Wu *et al.*, Multi-shape active composites by 3D printing of digital shape memory polymers. *Sci. Rep.* **6**, 24224 (2016).
52. Q. Zhang, K. Zhang, G. Hu, Smart three-dimensional lightweight structure triggered from a thin composite sheet via 3D printing technique. *Sci. Rep.* **6**, 22431 (2016).
53. L. Huang *et al.*, Ultrafast digital printing toward 4D shape changing materials. *Adv. Mater.* **29**, 1605390 (2017).
54. S. E. Bakarich, R. Gorkin, M. i. h. Panhuis, G. M. Spinks, 4D printing with mechanically robust, thermally actuating hydrogels. *Macromol. Rapid Commun.* **36**, 1211-1217 (2015).
55. C. P. Ambulo *et al.*, Four-dimensional printing of liquid crystal elastomers. *ACS Appl. Mater. Interfaces* **9**, 37332-37339 (2017).
56. A. Kotikian, R. L. Truby, J. W. Boley, T. J. White, J. A. Lewis, 3D printing of liquid crystal elastomeric actuators with spatially programed nematic order. *Adv. Mater.*, 1706164 (2018).
57. W. Li *et al.*, Flexible circuits and soft actuators by printing assembly of graphene. *ACS Appl. Mater. Interfaces* **8**, 12369-12376 (2016).
58. H. Fu *et al.*, Morphable 3D mesostructures and microelectronic devices by multistable buckling mechanics. *Nat. Mater.* **17**, 268-276 (2018).